Energy Harvesting from a Vortex Ring using Highly Deformable Smart Materials

by

Jia Cheng Hu

A thesis
presented to the University of Waterloo
in fulfillment of the
thesis requirement for the degree of
Master of Applied Science
in
Mechanical Engineering

Waterloo, Ontario, Canada, 2015

Author's Declaration

I hereby declare that I am the sole author of this thesis. This is a true copy of the thesis, including any required final revisions, as accepted by my examiners.

I understand that my thesis may be made electronically available to the public.

Abstract

Recently, the growing demand of compact energy harvesters for wireless sensor networks has lead to an increasing interest in exploring the energy harvesting capabilities of smart materials. Smart materials are a category of transducer that is able to convert dynamic structural deformations into electricity and vice versa. To investigate the feasibility and the potential of small-scale smart material-based harvesters to obtain energy from ambient fluid environments, interactions between a vortex ring and smart material structure are examined. Vortex rings are a class of coherent structure that is common in nature and act as a canonical representation of vortex structures.

Herein, two energy harvesting configurations are considered. First, energy transfer from a passing vortex ring to a cantilevered plate, which is oriented parallel to and offset from the vortex ring's path, is modeled and optimized. The three-dimensional problem is simplified to a two-dimensional problem using a novel method that maintains the loading characteristics of the vortex ring. Two-dimensional Kirchhoff-Love plate theory and two-dimensional potential flow theory are utilized to represent the solid and fluid, respectively. The coupled fluid-structure model is solved simultaneously and validated against published experimental data. Employing this analytical model, the optimization study aims at locating the resonance frequency with respect to the change in fluid and structure parameters. The dimensionless resonance frequency is established as a specific ratio between the plate's fundamental frequency and vortex convective time-scale using a classical moving point load analysis. The result of the optimization study provides a description and empirical formulation of the shift in dimensionless frequency as a result of various fluid and structure parameter adjustments.

In the second configuration, the energy harvesting potential of a vortex ring impacting an ionic polymer composite (IPMC) annulus is examined experimentally. The annulus is axis-symmetrically aligned with an incoming vortex ring that is generated by a piston/cylinder setup. The tip deflection of the annular energy harvester is measured with a laser displacement sensor, while the cross-sectional flow field is measured with particle imaging velocimetry and the electrical energy accumulated by the IPMC is estimated with the short-circuit current output. The experimental results unveiled that the annulus is first pulled by the vortex ring low pressure core, and then pushed upon impact. A secondary vortex ring is observed convecting away from the annulus. It is possibly formed out of the vortex induced vorticity at the annulus tip, while the incoming vortex ring is destroyed at impact. The experimental result is found to be in good agreement with an analytical solution.

Acknowledgments

First and foremost, I would like to extend my deepest gratitude to my mother, Qiao Qin Tian, who gave up everything she had in China and came to Canada for me to have a better education. She raised me in a foreign country by herself, and had to work two jobs for a roof over my head and food on my plate. I wouldn't be pursuing my passion of scientific research without her sacrifice and support.

I would also like to extend my deepest gratitude to my academic adviser, Professor Sean D. Peterson. He is always available to discuss and support my research, and has given me much freedom to develop my own research style. Outside of my academic study, he introduced me to daily exercising, swimming, running, cycling, triathlon, and NFL. More importantly, he guided me to become a better and more confident person with his infinite patience. He means more than a adviser to me, he is like the father I always wanted. He is an excellent wizard of science, mentor and friend.

I would like to extend my appreciation to good friend Dr. Chekema Prince, who is like a big sister to me. She is a great person to talk when I have problems. Her encouragement and advices help me to push for the next level. Additionally, her excellent taste in fashion is a great resource for me.

I would like to thank Kristine Meier, who helped me though my difficult time. She is an excellent counsellor, and I will always be grateful for all that you have done to help me.

I would like to thank my friend Benjamin Quinn for supporting me for pursuing my graduate stuff and teaching me how to play Civilization 5. I would like to thank my friend Ramin Manouchehri for his great advises on thesis writing and teaching how to play Hearthstone. I would to thank my friend Andrew Buckrell for his advises on my graduate study and exercises.

I would like to thank my colleagues from the Dynamical Systems Laboratory at New York University. I would like to thank Professor Maurizio Porfiri for his input on my work. I am a big fan of his research. I would like to thank Dr. Youngsu Cha for his assistance on my research with ionic polymer-metal composite. I would like to thank Hubert Kim for teaching me about ionic polymer-metal composite fabrication and the great discussions. I would like to thank Mohammad Jalalisendi, Adel Shams and Steven Osma for letting stay at their place when I am in New York.

Lastly, I would like to thank my fellow graduate students, Sahil Mahey, Eugene Zivkov, John Kurelek, Ajith Airody, Supun Pieris, Matt McMaster, Jon Deng, Jennifer Book, David Sommer, Brian Kettlewell, and Jeff McClure for the interesting discussions and entertainment. Friday beer is always a good source of stress relief.

Table of Contents

List of Figures

List of Tables

Nomenclature

Chapter 2 Nomenclature

Re	Reynolds number	$[-]$
Γ_r	Vortex ring circulation	$[\mathrm{m^2/s}]$
a_r	Vortex ring radius	$[\mathrm{m}]$
b_r	Vortex ring core radius	$[\mathrm{m}]$
V_c	Vortex ring/pair convection speed	$[\mathrm{m/s}]$
h_r	Initial distance from the vortex ring center axis to the undeformed plate plane	$[\mathrm{m}]$
T	Plate thickness	$[\mathrm{mm}]$
W	Plate width	$[\mathrm{m}]$
L	Plate length	$[\mathrm{m}]$
x	Cartesian coordinate x-axis	$[\mathrm{m}]$
y	Cartesian coordinate y-axis	$[\mathrm{m}]$
z	Cartesian coordinate z-axis	$[\mathrm{m}]$
t	Time	$[\mathrm{s}]$
Υ	Plate effective Young's modulus	$[\mathrm{GPa}]$
ϱ	Plate mass density per unit volume	$[\mathrm{kg/m^3}]$
δ	Plate deflection	$[\mathrm{m}]$
B	Plate bending stiffness per unit width	$[\mathrm{Nm}]$
M	Plate mass per unit surface area	$[\mathrm{kg/m}]$
C	Plate structural damping	$[\mathrm{Ns/m}]$
$[\![p]\!]$	Pressure difference between top and bottom of the plate	$[\mathrm{Pa}]$
L_0	Length scale	$[\mathrm{m}]$
V_0	Velocity scale	$[\mathrm{m/s}]$
t_0	Time scale	$[\mathrm{s}]$
p_0	Pressure scale	$[\mathrm{Pa}]$

ρ	Fluid density	[kg/m^3]
β	Dimensionless plate bending stiffness	[−]
μ	Dimensionless plate mass	[−]
η	Dimensionless plate structural damping	[−]
Γ_p	Vortex pair circulation	[m^2/s]
a_p	Vortex pair vortices initial separation distance	[m]
h_p	Initial distance from the vortex pair midpoint to the undeformed plate plane	[m]
ζ	Complex coordinate	[−]
w	Complex velocity	[m/s]
i	Imaginary number	[−]
ζ_1	Vortex pair top vortex complex position	[m]
ζ_2	Vortex pair bottom vortex complex position	[m]
Λ	Dimensionless vortex pair vortices initial separation distance	[−]
γ	Plate vortex sheet vorticity distribution	[m/s]
x_0	Vortex pair initial x-axis locaiton	[m]
H	Dimensionless initial distance from the vortex pair midpoint to the undeformed plate plane	[−]
u_r	Vortex ring axial velocity	[m/s]
v_r	Vortex ring radial velocity	[m/s]
Y	Vortex ring Biot-Savart law constant	[−]
H_r	Dimensionless initial distance from the vortex ring center axis to the undeformed plate plane	[−]
$\mathcal{A}$	Vortex ring Biot-Savart law constant	[−]
$\mathcal{B}$	Vortex ring Biot-Savart law constant	[−]
$\mathcal{C}$	Vortex ring Biot-Savart law constant	[−]
Λ_r	Dimensionless vortex ring vortices initial separation distance	[−]
λ	Vortex ring Biot-Savart law constant	[−]
I_1	Vortex ring Biot-Savart law constant	[−]
I_2	Vortex ring Biot-Savart law constant	[−]
$\mathcal{K}$	Complete elliptic integral of the first kind	[−]
$\mathcal{E}$	Complete elliptic integral of the second kind	[−]
u_p	Vortex pair axial velocity	[m/s]
v_p	Vortex pair radial velocity	[m/s]
Λ_p	Dimensionless vortex pair vortices initial separation distance	[−]
H_p	Dimensionless initial distance from the vortex pair midpoint to the undeformed plate plane	[−]
p_r	Vortex ring pressure	[Pa]

p_p	Vortex pair pressure	[Pa]
U	Conversion constant	$[-]$
F	Conversion constant	$[-]$
f	Net force per unit width	$[N/m]$
E	Plate energy	$[J]$
ω_p	Characteristic frequency of the pressure loading	[rad/s]
$\omega_\mathrm{i}^\mathrm{res}$	Resonance frequency of ith vibration mode of the plate	[rad/s]
Ω	Dimensionless natural frequency of the 1st vibration mode of the plate	$[-]$

Chapter 3 Nomenclature

r	Cylindrical coordinate radial axis	$[-]$
θ	Cylindrical coordinate azimuthal axis	$[-]$
x	Cylindrical coordinate longitudinal axis	$[-]$
a_i	Initial vortex ring core radius	[mm]
a	Vortex ring core radius	[mm]
R_i	Initial vortex ring radius	[mm]
R	Vortex ring radius	[mm]
Γ	Vortex ring circulation	[mm^2/s]
h	Annulus thickness	[mm]
R_o	Annulus outer radius	[mm]
R_i	Annulus inner radius	[mm]
t	Time	[s]
ξ	Distance between the vortex ring and the annulus	[mm]
δ	Annulus deflection	[mm]
ρ	Ionic polymer-metal composite mass density per unit volume	[kg/m^3]
D	Ionic polymer-metal composite bending stiffness	[Nm^2]
$[\![p]\!]$	Total pressure difference across the annulus	[Pa]
E	Ionic polymer-metal composite Young's modulus	[MPa]
ν	Ionic polymer-metal composite Poisson's ratio	$[-]$
ϱ	Fluid density	[kg/m^3]
μ	Mass ratio	$[-]$
K	Dimensionless bending stiffness	$[-]$
ϕ_+	The potential function for $x > 0$ half-space	$[-]$
ϕ_-	The potential function for $x < 0$ half-space	$[-]$
ϕ_vr	The potential function for vortex ring	$[-]$

ϕ_{img}	The potential function for image vortex ring	$[-]$
ϕ_{ap}	The potential function for aperture correction	$[-]$
J_α	Bessel function of the first kind of order α	$[-]$
β	Annulus hole size to vortex ring initial radius ratio	$[-]$
u	Cylindrical coordinate longitudinal velocity	[mm/s]
v	Cylindrical coordinate radial velocity	[mm/s]
U	Velocity magnitude	[mm/s]
$[\![p_0]\!]$	Pressure difference across the annulus from potential flow	[Pa]
H	Annulus added mass effect	[Pa]
R_{IPMC}	Ionic polymer-metal composite resistance	$[\Omega]$
C_{IPMC}	Ionic polymer-metal composite capacitance	[mF]
V_{d}	Ionic polymer-metal composite model voltage source	[V]
γ	Ionic polymer-metal composite sensing gain	[Vmm]
κ	Ionic polymer-metal composite mean curvature	[1/mm]
I_{sc}	Ionic polymer-metal composite short circuit current	[mF]
E_{vr}	Vortex ring energy	$[\mu\text{J}]$
E_{IPMC}	Ionic polymer-metal composite harvested energy	[nJ]
Δ_{n}	Annulus nth mode shape	$[-]$
λ_{n}	Annulus nth mode eigenvalue	$[-]$
a_{n}	Annulus nth mode amplitude	$[-]$
$\mathbf{u}$	Fluid velocity vector	[mm/s]
C	Circulation integral contour	$[-]$
Γ_{pre}	Pre-impact vortex ring circulation	[mm^2/s]
Γ_{post}	Post-impact vortex ring circulation	[mm^2/s]
δ_{max}	Maximum annulus deflection	[mm]
I_{max}	Maximum ionic polymer-metal composite short circuit current	$[\mu\text{A}]$

Chapter 1

Introduction

Research interest in the development of small-scale energy harvesting methods is primarily motivated by the advancements in ultra low power electronic designs that allow miniature wireless sensor nodes to be powered by built-in energy scavengers. One particular interesting subset of small scale energy harvesting involves extracting energy directly from fluid motion around the harvester via fluid-structure interactions (FSI). Due to the modeling complexity of this multi-physics phenomena, it is difficult to optimize the harvester to meet the demanding requirements of the current state-of-the-art wireless node. The aim of this thesis is to examine analytically and experimentally the interaction between a highly deformable material and a single vortex ring. This simplified scenario provides insights into the multi-physics coupling and vortex dynamics that can inform the design of small-scale fluidic energy harvesters for use in more complex flow environments.

1.1 Small Scale Energy Harvesting

For an overview of small scale energy harvesting as a potential source for powering remote wireless sensor networks, the current state of wireless sensor nodes, smart material harvesters, and ambient energy harvesting techniques from fluid environments are briefly described in the following sections.

1.1.1 Wireless Sensor Network

Wireless sensor networks (WSN) have become a reality due, in part, to modern advancements in integrated circuit (IC) designs and complementary metal-oxide-semiconductor (CMOS) processes. These advances are making many exciting applications possible in the near future, such as environmental monitoring and ambient intelligence [1]. Each node in the network is a self-contained unit capable of wireless sensing, communication, and computation. These nodes work in a dense ad-hoc network with a transmission range of 10 meters for each node [2]. Comparing to the rest of the powering solutions for WSN, mainly, battery and wireless power transmission, the built-in energy scavenger is the most attractive option. For the battery option, the limited energy storage capacity determines the lifetime of a node and battery replacement costs would be enormous for a massive WSN deployment, whereas a self-sustaining node eliminates such concerns [3]. For the wireless power transmission using radio frequency (RF) radiation, Federal Communications Commission (FCC) and health concerns limit the amount power that is allowed to be transmitted [3]. In the past decade, a few prototypes of wireless sensor nodes have been successfully developed. A University of California Berkeley research group developed

a wireless node called PicoCube for monitoring vehicle tire pressure [4]. It has a volume of 1 cm^3, an average power consumption of 6 μW, and is powered by a vibration-based energy harvester made out of dielectric elastomers. A research group at the University of Michigan developed a mm^3-scale wireless intraocular pressure monitor powered by a solar cell that harvests light entering the eye, which provides up to 80.6 nW and only requires 1.5 hours of sunlight or 10 hours of indoor lighting per day to operate [5]. NNT Corporation in Japan developed a 1 cm^3 event-driven wireless node that only requires 8 μJ to send 36-bit data per event using energy stored in its capacitor, which is harvested from a solar source [6]. The GENESI project lead by the University of Rome La Sapienza developed a hybrid energy supply for structural health monitoring WSN [7]. The power supply consists of a 800mAh battery, a fuel cell, a solar energy harvester and a wind energy harvesting component. It can achieve a sampling rate of 0.75% duty cycle using energy harvesters only, and 1.5% duty cycle with the help of the fuel cell. As these successes highlight, there is considerable promise for small-scale electronic devices that can be powered via energy extraction from the local environment; this is still, however, a relatively new and immature field that requires continuing efforts from the research community to improve the design of each level of the system, including exploration of alternative energy harvesting methods and modalities.

1.1.2 Smart Material-Based Harvesters

Despite the advantages of self-powered wireless sensors, there are also significant challenges when it comes to the design of the energy scavenging unit. Unlike other designs, the self-

powered design is highly dependent on the surrounding environment and the vast variety of energy sources, which includes mechanical vibrations, thermal gradients, fluid flow, and solar power [8]. Each scenario requires detailed study to facilitate harvester design and optimization, which leads to the large, interdisciplinary research and development effort on the topic of energy harvesting.

The present study focuses on energy harvesting from fluid sources using a subset of electromechanical transducers, commonly referred as the smart materials. They are high deformable materials that required time-dependent forcing from the fluid sources to generate electrical power. Piezoelectrics and ionic polymer-metal composite (IPMC) are two popular choices of such transducers. Piezoelectrics are materials that exhibit direct and converse piezoelectric effects. In short, the direct piezoelectric effect is an accumulation of electrical charges at the electrodes when the material is subjected to the dynamic mechanical strain; the converse piezoelectric effect is the mechanical deformation experienced by the material when a voltage is applied to the electrodes [9]. The direct piezoelectric effect is the principal mechanism for energy harvesting applications; however, due to voltage feedback, the converse piezoelectric effect is still taking place when the material is used for purely sensing purposes. In other words, piezoelectric materials have a strong bidirectional electromechanical coupling, and it must be considered in the modeling for energy harvesting applications [10, 11]. Design of a piezoelectric energy harvester commonly consists of piezoelectric patches attached to one (unimorph) or both (bimorph) sides of a deformable host beam [10]. Common options of piezoelectric materials are lead zirconate titanate (PZT) and polyvinylidene difluoride (PVDF) [12]. Figure 1.1a shows a cantilevered bimorph Piezoelectric energy harvester design. Piezoelectric patches are glued to both sides
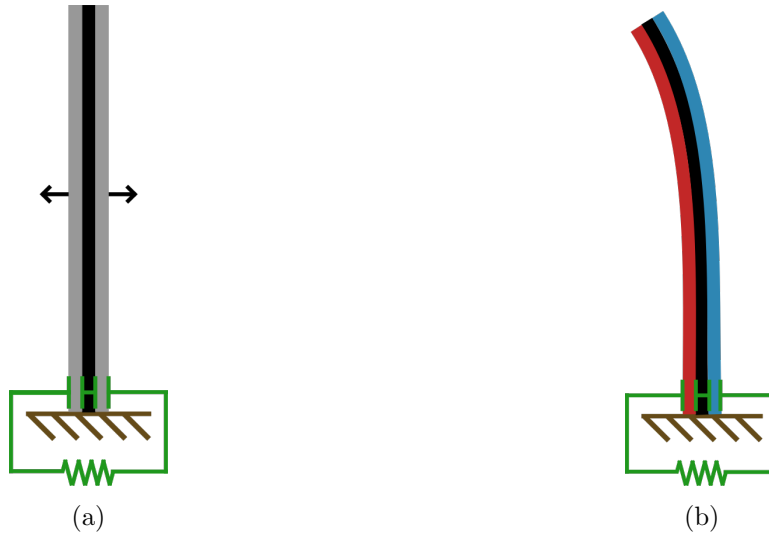
Figure 1.1: Schematic of a bimorph Piezoelectric energy harvester (a) in undeflected state, and (b) in deflected state. The host plate is colored in black, resistive load is colored in green, and arrows indicates piezoelectric material poling direction. Unstrained piezoelectric patch is colored in grey in (a), and the blue and red colors of the piezoelectric patch in (b) indicate opposite signs of strain encountered by the patch.

of a host plate with opposite poling directions connected in a series. A resistive load is commonly used to estimate the energy harvesting potential. When the harvester sustains deflection, the patches are mechanically strained with opposite sign, indicated by the blue and red colors in Figure 1.1b, thus needing opposite poling directions for a series electrical connection. On the other hand, IPMCs are a type of electroactive ion-infused polymer [13]. It is capable of two-way electromechanical coupling that resembles piezoelectric materials. A schematic of an IPMC energy harvester setup is shown in Figure 1.2. Energy harvesting capability is estimated from short circuit current produced by the IPMC using an inverting operational amplifier [14–18]. The structure of an IPMC consists of 5 layers. The center layer is the electrically charged polymer (grey region in Figure 1.2) commonly made out
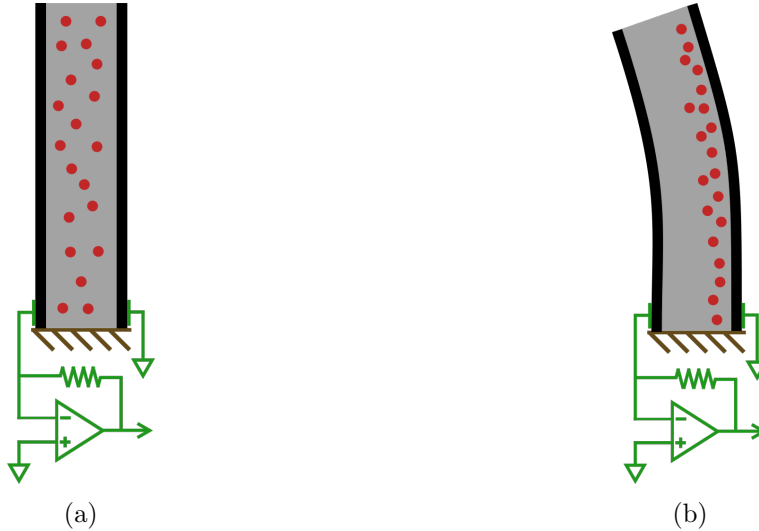
Figure 1.2: Schematic of an IPMC energy harvester setup (a) in undeflected state, and (b) in deflected state. The electrodes are colored in black, electroactive polymer is colored in grey, mobile ions are colored in red, and measurement circuit is colored in green.

of Nafion 117, and it is neutralized by mobile ions (red dots in Figure 1.2); the outer layers are electrodes commonly made out of Platinum (black region in Figure 1.2); the layer between electrode layer and the polymer is a composite layer consisting of a mixture of both platinum and polymer (not shown in Figure 1.2) [13, 19, 20]. Note that IPMC energy harvester does not require a host plate. Electrical sensing occurs when the mobile ions in the polymer membrane are redistributed by mechanical deformation, as shown in Figure 1.2b, which leads to charge accumulation near the electrodes [13, 19, 20]. When the mobile ions are redistributed by an electric field generated by a voltage difference applied to the electrodes, a number of concurrent microscopic events occurs that result in mechanical deformation [13, 19, 20]. Unlike piezoelectric materials, IPMCs have a much weaker electromechanical coupling coefficient. In the application of energy harvesting, its

electrical to mechanical feedback is negligible [14,16,20]. For the remainder of the thesis, a weak electromechanical coupling is assumed; this allows the simplification of the three-way electrical-mechanical-fluidic coupling and purely focus on the dynamics of FSI.

1.1.3 Ambient Fluidic Energy Harvesting

Fluidic energy is one of the major source of green energy, which provides 3619 TWh and 501 TWh world-wide in 2012 from hydro and wind, respectively [21]. The current study focuses on small-scale ambient fluidic energy harvesting methods that utilize fluid-induced vibration on highly deformable smart materials, due to its advantage of compactness and simple construction. The working principles of the fluid induced vibrations methods have three main categories: vortex induced vibration (VIV), aeroelasticity, and turbulent induced vibration (TIV).

1.1.3.1 Vortex Induced Vibration

VIV makes use of the alternating pressure loading generated by passing vortices. The most popular option is the Kármán vortex street behind a bluff body in a free stream. Taylor *et al.* placed a cantilevered soft PVDF piezoelectric strip behind a plate with the tip pointing away from the body and demonstrated a capability of producing 1 W with a 1 m/s flow rate in water [22]. Bischur *et al.* developed a similar harvesting configuration, but using a more rigid PZT piezoelectric material that is able to harvest 2 mW from an 8 m/s flow in a wind channel [23]. Gao *et al.* demonstrated that a PZT unimorph cantilevered plate with a cylindrical extension can harvest up to 30 μW from a 5 m/s wind speed fan [24]. Akaydin

et al. investigated a configuration, where the cantilevered plate is behind a cylinder with its free end pointing at the cylinder, that is able to provide up to 4 μW from a 7.23 m/s free stream [25]. They also examined a self-exciting energy harvester with a cantilevered plate that has a cylindrical tip; it can generate 0.1 mW from a 1.192 m/s free stream. However, the performance of VIV from the wake of a bluff body is significantly impacted by highly turbulent free streams [26].

1.1.3.2   Aeroelasticity

Galloping is a type of self-excited aeroelastic phenomenon that has low frequency and large magnitude oscillations normal to the free stream [27]. The energy harvesters utilizing galloping motion have similar designs to some of the VIV energy harvesters, usually consisting of a cantilevered plate with a non-circular tip or extension. Sirohi *et al.* used a PZT bimorph cantilevered plate with a D-section extension to get a maximum output of 1.14 mW from a 4.7 m/s wind [27], and with a triangle-section tip to get a maximum output of 53 mW from a 5.2 m/s wind [28]. Yang *et al.* harvested 8.4 mW from a 2.5 m/s wind using a PZT bimorph cantilevered plate with a square-section tip [29]. Fluttering is also a type of self-excited aeroelastic phenomenon that commonly occurs in a flapping flag motion. Li *et al.* achieved 615 μW using cross-flow fluttering with a cantilevered PVDF plate [30]. Giacomello *et al.* harvested 0.1 nW from a heavy flapping flag that hosted small IPMC strips placed in a steady water channel with flow rate in the range of $0.6 - 1.1$ m/s [31]. Michelin *et al.* optimized energy harvesting with a flapping flag using Lighthill's theory [32].

1.1.3.3 Turbulent Induced Vibration

Turbulent flow is the most common fluid flow state in nature, but TIV harvesting is the hardest to study due to its randomness and the complex vortex-structure interactions. Akaydin *et al.* investigated energy harvesting from a turbulent boundary layer using the same cantilevered piezoelectric plate employed in the study of harvesting behind a cylinder. They managed an output of 0.06 μW, which is significantly lower compared to the cylinder case of 4 μW [25]. Hobeck *et al.* harvested 1 mW per cantilever with an 11.5 m/s mean flow rate and 1.2 μW with 7 m/s mean flow rate, using a series of PZT and PVDF strips, respectively [33].

The fluid to structure energy transfer efficiency of these harvesters still have room to improve. Out of the three discussed methods, VIV and TIV are difficult to analyze and optimize due to the fluid-structure coupling and the strong viscous effects that occur in many cases. Thus, it is instructive to examine the detailed interaction process with a single vortex filament to inform the design of VIV harvesters and provide some insights into more complex vortex-structure interactions for TIV harvesters.

1.2   Vortex-Structure Interaction

To investigate the vortex dynamics and fluid-structural coupling of the interaction between a single vortex filament and a highly deformable structure, vortex rings are utilized in the present study. An overview of vortex rings and recent studies of vortex-structural interaction are briefly described in the following sections.

1.2.1 Vortex Rings

Vortex rings are a class of self-convecting coherent fluid structures commonly found in nature. For instance, vortex rings are formed during the discharge of blood in the human heart [34], as a result of a flapping fish tail [35] and the initiation of an impulsively started jet. In addition to their ubiquity in nature, vortex rings serve as a fundamental element in the general study of vortex dynamics due to their amenability to analytical exploration, and the ease with which they can be generated experimentally. Their formation process [36–40] and dynamics [41–46] are well documented. They also have been studied extensively for vortex dynamics [47–55], instabilities [56–58], turbulence [59–63], and interactions with rigid structures [64–70].
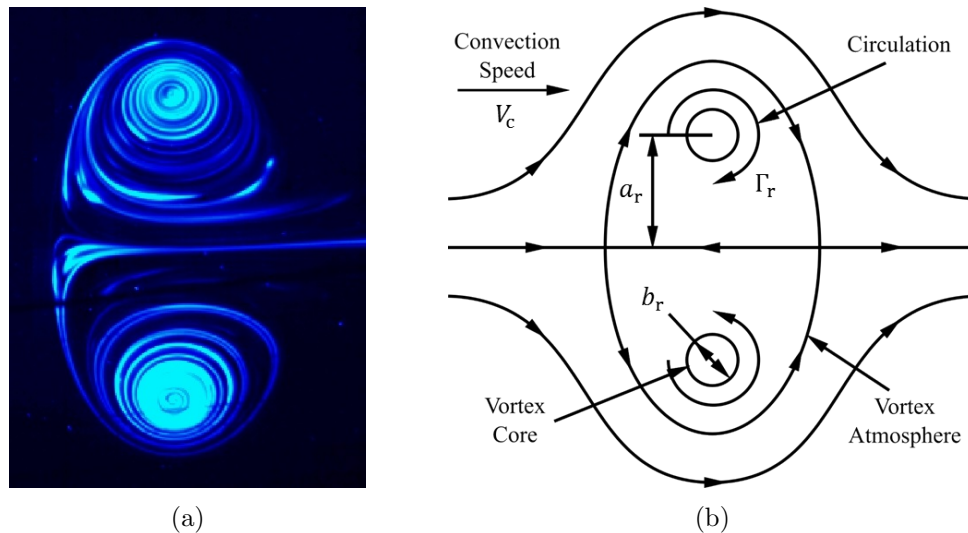

| (a) | (b) |

Figure 1.3: Laminar thin core vortex ring (a) cross-section flow visualization and (b) its structure shown with respect to the moving frame at the center of the vortex ring.

The type of vortex rings employed in the present study is laminar thin core vortex

rings, see Figure 1.3a. Its structure, as shown in Figure 1.3b, consists of a toroidal vortex core inside of a vortex atmosphere, and it moves through an otherwise quiescent fluid environment at convection speed V_c. The inside of the vortex atmosphere is a closed volume of fluid that circulates the vortex core [71]. Its vorticity distribution is in the form of a Gaussian distribution with the maximum vorticity at the center of the core and a net circulation of Γ_r [71]. The core region is commonly defined as the area that encompasses about half of the total vorticity [71]. The flow field outside of the vortex atmosphere can be calculated using potential flow as a moving ellipsoid. The primary parameters that determines the dynamic properties are ring radius a_r, core radius b_r, and circulation Γ_r [71]. The thin core notion refers to vortex rings that have a low core to ring radius b_r/a_r [43]. The advantage for this study of having a thin core is that it is relatively easy to analyze and model due to its concentrated vorticity field. Additionally, potential flow methods can resolve the thin core vortex ring's flow field without difficulty, except within the vortex core.

1.2.2 Vortex-Deformable Structure Interaction

Recently, there have been a few studies that have employed vortex rings as the energy source for small-scale energy harvesting. Peterson and Porfiri examined the direct impact of a vortex ring with a cantilevered IPMC and found that $0.2 - 1.5$ nJ can be acquired from the impact of a vortex ring with energy in the range of $7 - 18$ mJ. They also concluded that the interaction is split into two stages of far-field and near-field. In the far-field phase, the plate is slowly deflected as the vortex ring approaches; then, in the near-field phase, as

the vortex ring reaches the plate, there is a sudden increase in the plate deflection while the vortex ring impacts and subsequently breaks down [72]. They further examined the interaction by modeling it with a potential flow method in a two-dimensional setting, and found that the energy transferred to the plate increases with increasing vortex circulation and decreasing plate to fluid inertia ratio [73]. Furthermore, they modelled the interaction numerically in two-dimensions with a vortex dipole impacting the tip of a semi-infinite plate to examine the vortex dynamics in the presence of viscosity, and discovered that the plate split the dipole into two portions, where one portion interacted with vorticity generated along the plate, and the other portion interacted with vorticity shed from the tip [74]. Lastly, Zivkov *et al.* examined a vortex dipole impacting the tip of a deformable plate, and discovered that maximum deflection is not significantly effected by the vortex dipole's Reynolds number, but the subsequent response varies with the Reynolds number [75].

Goushcha *et al.* investigated the cases where a single or multiple vortex rings passed by a cantilevered deformable plate oriented parallel to the vortex ring's path. They found that the passing vortex ring first pushes on the plate as it approaches, then pulls on the plate as the low-pressure vortex core passes over the plate. They also observed an increase in the deflection by matching the fundamental frequency of the plate with the interval between the subsequent vortex rings in a train [76].

Alben examined the inviscid interaction between a point vortex and a deformable surface that is either an infinite straight line or a circle [77]. He found that the deformation of the infinite straight line surface enhances the flow at the surface and accelerates the vortex. He further found that there is a mutual amplification between the deflection and force induced by the deflection as the vortex approaches the circular surface. Alben later

12

investigated the attraction between a finite deformable flexible plate and a point vortex in an inviscid fluid [78]. He found that in the vicinity of a vortex, the deformable plate is pulled toward the vortex, due to the low pressure of the vortex core, resulting in a collision, unlike a rigid plate, where the vortex stays in a stable orbit. To the best of the author's knowledge, the studies mentioned above are the only studies that aim to address the coupling behaviours and vortex dynamics of the interaction between a deformable plate and vortices; thus there is a need for further understanding of the complex interaction to optimize the energy harvesters.

1.3   Study Objectives

The present study focuses on unitize vortex rings to further investigate vortex-deformable structure interactions and to address the following specific research objectives:

1. analytically examine and optimize the energy transfer of the harvesting experiment by Goushcha *et al.* [76] where a single vortex ring passes by a cantilevered deformable plate

2. experimentally examine the vortex dynamics and energy harvesting capability of a vortex ring coaxially impacting deformable annular disk.

1.4 Thesis Overview

The thesis is organized as follows: Chapter 2 analytically studies and optimizes the fluid to structure energy transfer of the configuration introduced by Goushcha *et al.* [76], using a fully coupled two-dimensional fluid-structure potential flow method proposed by Peterson and Porfiri [73]. Chapter 3 reports on the experimental investigation of the energy harvesting capability of impacting a vortex ring to an IPMC annular disk. Finally, concluding remarks and recommendations are discussed in Chapters 5 and 6, respectively.

Chapter 2

Energy transfer between a passing vortex ring and a flexible plate in an ideal quiescent fluid [1]

In a timely experimental study conducted by Goushcha *et al.* [76], the energy harvesting potential of single and multiple vortex rings passing by a cantilevered plate oriented parallel to, and offset from the vortex ring trajectory was explored. The vortex ring was generated by a speaker/cylinder setup in otherwise stagnant air, and it interacted with a flexible cantilevered polycarbonate plate. The strain at the clamped edge was measured via a small strain gauge, and time-resolved particle image velocimetry (PIV) was used to obtain information about the flow kinematics. The pressure loading on the plate was subsequently

---

[1]The contents of this chapter is published in the Journal of Applied Physics [79]. Professor Sean D. Peterson and Professor Maurizio Porfiri provided feedback and direction throughout the project.

inferred from the flow kinematics using both control volume and direct integration methods. The structural vibration of the cantilevered plate was found to be influenced by the pressure fluctuation caused by the passing vortex ring. Subsequent rings could be timed such that they either enhanced or mitigated the vibration amplitude of the beam, which is related to the energy harvesting potential of the configuration.

In this chapter, we model the energy harvesting configuration introduced and explored experimentally by Goushcha *et al.* [76] using a two dimensional potential flow model [73]. Specifically, the interaction between a single vortex pair and a cantilevered deformable plate in an otherwise quiescent ideal fluid is proposed as a template for performing optimization studies on the vortex-deformable structural energy transfer in which viscous fluid forces are negligible, in pursuit of maximizing the energy scavenger's harvesting potential. This paper is organized as follows: the problem is formulated and the potential flow model is introduced in §2.1; a scheme to proxy a vortex ring through a vortex pair is developed in §2.2; the model is validated against published experimental data in §2.3; and optimization of the energy transfer based upon the analytical is model is presented in §2.4.

2.1 Problem Formulation

Here, we analytically explore the problem addressed experimentally by Goushcha *et al.* [76] of a vortex ring passing over a cantilevered plate oriented parallel to, and offset from, the path of a vortex ring in an otherwise quiescent fluid, see Figure 2.1a. The vortex ring has ring diameter a_r, core diameter b_r, circulation Γ_r, initial distance of the ring center axis to the plane of the undeformed plate h_r, and initial convection speed V_c. A Cartesian

16

coordinate system is defined at the geometric center of the plate, with x oriented along the plate pointing from the fixed to the free end, y oriented normal to the plate in the undeformed state and pointing towards the vortex ring, and z forming a standard right-handed coordinate system, see Figure 2.1a. The plate has length L, width W, and thickness T, and is clamped at $x = -L/2$.
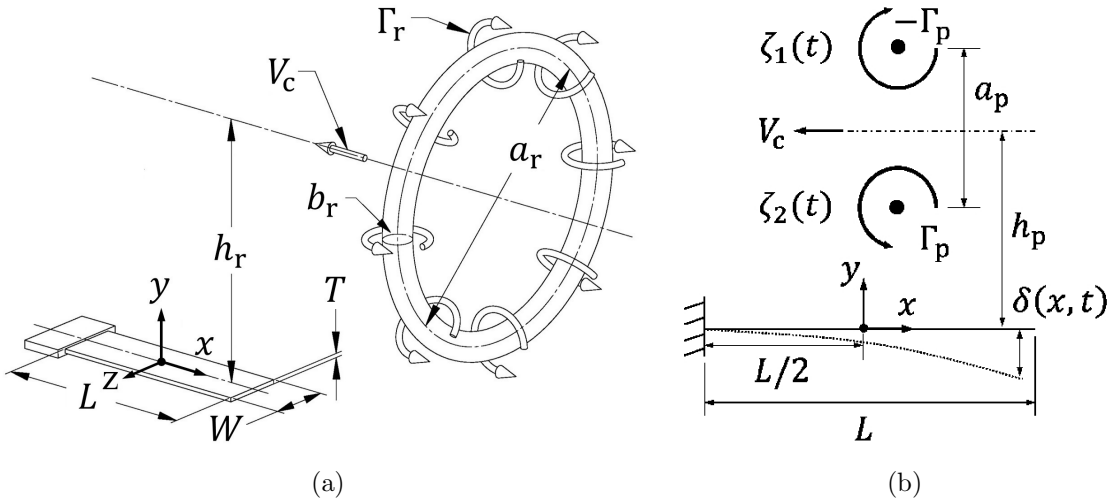
Figure 2.1: (a) Schematic of the experiment performed by Goushcha *et al.* [76] of a vortex ring passing over a cantilevered plate; and (b) two-dimensional vortex pair-based representation of the experiment.

We assume that viscous dissipation of the vortex core while passing over the plate is negligible, due to the short interaction time of the ring with the plate; thus, the circulation Γ_r is assumed to be constant throughout the interaction. We further assume that the vortex ring core diameter b_r is small in comparison with its overall diameter a_r [43], and the plate and the vortex ring are sufficiently far away from one another such that the interaction between the vortex core and the induced vorticity on the plate is negligible.

With these assumptions, the surrounding fluid is modeled as incompressible, inviscid, and irrotational, except in the core of the vortex ring. We hypothesize that the plate length is much larger than its thickness and that the plate vibration is of small amplitude and confined to the xy-plane. The effective Young's modulus of the plate and the mass density per unit volume are Υ and ϱ, respectively. As such, the plate is modeled as a Kirchhoff-Love plate [80] undergoing cylindrical bending in response to the applied fluid loading. The structural damping of the plate is captured using a distributed viscous damping model [81]. The governing equation for the plate dynamics is

$$M\ddot{\delta}(x,t) + C\dot{\delta}(x,t) + B\delta^{\mathrm{IV}}(x,t) = -[\![p]\!](x,t) \tag{2.1}$$

where δ is the plate deflection, $B = \Upsilon T^3/12$ is the plate bending stiffness, $M = \varrho T$ is the plate mass per unit surface area, C quantifies the structural damping, and $[\![p]\!]$ is the pressure difference between the top (positive y-plane) and bottom (negative y-plane) of the plate due to the fluid. The roman numeral indicates the order of differentiation with respect to x, while a dot indicates differentiation with respect to time t. The initial conditions for the plate are $\delta(x,0) = \dot{\delta}(x,0) = 0$, while the fixed-free boundary conditions are $\delta(-L/2,t) = \delta^{\mathrm{I}}(-L/2,t) = \delta^{\mathrm{II}}(L/2,t) = \delta^{\mathrm{III}}(L/2,t) = 0$. We note that Equation (2.1) only applies to weakly electromechanically coupled harvesters, such as ionic polymer metal composites [16,82,83]. Materials with stronger coupling, such as piezoelectrics, would require taking into consideration bidirectional effects, whereby the electrical response would directly influence the mechanical deformation, and vice versa [10, 11].

Employing $L_0 = L/2$ as the length scale, $V_0 = V_c$ as the velocity scale, $t_0 = L_0/V_0$ as

the time scale, and $p_0 = \rho V_0^2$ as the pressure scale, where ρ is the fluid density, Equation (2.1) can be expressed in dimensionless form as

$$\mu \ddot{\hat{\delta}}(\hat{x}, \hat{t}) + \eta \dot{\hat{\delta}}(\hat{x}, \hat{t}) + \beta \hat{\delta}^{\mathrm{IV}}(\hat{x}, \hat{t}) = -[\![\hat{p}]\!](\hat{x}, \hat{t}) \tag{2.2}$$

where $\beta = B/(\rho V_0^2 L_0^3)$ is the ratio of the plate restoring force to the applied fluid loading, $\mu = M/(\rho L_0)$ is the plate mass to fluid mass ratio, and $\eta = C/(\rho V_0)$ relates the structural damping to the applied fluid loading. A hat over a variable indicates that it is dimensionless. The dimensionless initial and boundary conditions are $\hat{\delta}(\hat{x}, 0) = \dot{\hat{\delta}}(\hat{x}, 0) = 0$ and $\hat{\delta}(-1, \hat{t}) = \hat{\delta}^{\mathrm{I}}(-1, \hat{t}) = \hat{\delta}^{\mathrm{II}}(1, \hat{t}) = \hat{\delta}^{\mathrm{III}}(1, \hat{t}) = 0$, respectively.

In order to gain analytical traction on the vortex ring/plate interaction problem depicted in Figure 2.1a, we recast the three-dimensional problem into a two-dimensional analog by assuming that the diameter of the vortex ring a_{r} is much larger than the width of the plate W. Under this assumption, the vortex ring curvature in the vicinity of the plate is small. Furthermore, we neglect three-dimensional effects along the edges of the plate. A schematic of the two-dimensional model is presented in Figure 2.1b. In two-dimensions, the vortex ring is represented by a pair of counter-rotating free vortices with initial separation, convection speed, and circulation of a_{p}, V_{c}, and Γ_{p}, respectively. The midpoint between the pair is initially at a distance h_{p} from the plane of the undeflected plate. We note that the convection speeds of both the vortex ring and pair are denoted by the same variable, V_{c}, which will be discussed in §2.2. For the remainder of the manuscript, the subscript r will denote vortex ring properties, while a subscript p will be employed to denote properties of the vortex pair.

For convenience, we introduce the complex coordinate $\zeta = x + iy$ and the complex velocity $w = u - iv$, where u and v are the velocity components in the respective x and y directions, and $i = \sqrt{-1}$. The positions of the two vorticies in the vortex pair are given by ζ_1 and ζ_2, respectively, see Figure 2.1b. Following Peterson and Porfiri [73], the velocity field at any location ζ in the domain at given time t in non-dimensional form is

$$\hat{w}(\hat{\zeta}, \hat{t}) = \frac{i}{2\pi} \left[2\pi\Lambda \left(\frac{1}{\hat{\zeta} - \hat{\zeta}_1(\hat{t})} - \frac{1}{\hat{\zeta} - \hat{\zeta}_2(\hat{t})} \right) - \int_{-1}^{1} \frac{\hat{\gamma}(\alpha, \hat{t})}{\hat{z} - \alpha} \, d\alpha \right] \tag{2.3}$$

where $\Lambda = a_p/L_0$. The first term on the right hand side of Equation (2.3) is the contribution from the vortex pair, while the second term is the velocity induced by a bounded vortex sheet whose vorticity distribution is given by $\hat{\gamma}(\alpha, \hat{t})$, which represents the plate in the fluid domain. We note that the relationship between the vortex circulation and the pair convection speed, $V_c = \Gamma_p/(2\pi a_p)$, is employed in the derivation and subsequent non-dimensionalization of Equation (2.3), see Ref. [73].

The kinematics of each vortex in the pair is governed by the desingularized velocity [84] at each respective vortex center as

$$\dot{\hat{\zeta}}_1(\hat{t}) = \text{Conj} \left\{ \frac{i}{2\pi} \left[-\frac{2\pi\Lambda}{\hat{\zeta}_1(\hat{t}) - \hat{\zeta}_2(\hat{t})} - \int_{-1}^{1} \frac{\hat{\gamma}(\alpha, \hat{t})}{\hat{\zeta}_1(\hat{t}) - \alpha} \, d\alpha \right] \right\} \tag{2.4a}$$

$$\dot{\hat{\zeta}}_2(\hat{t}) = \text{Conj} \left\{ \frac{i}{2\pi} \left[\frac{2\pi\Lambda}{\hat{\zeta}_2(\hat{t}) - \hat{\zeta}_1(\hat{t})} - \int_{-1}^{1} \frac{\hat{\gamma}(\alpha, \hat{t})}{\hat{\zeta}_2(\hat{t}) - \alpha} \, d\alpha \right] \right\} \tag{2.4b}$$

where $\text{Conj}(\cdot)$ represents complex conjugation, and $\dot{\hat{\zeta}}_1$ and $\dot{\hat{\zeta}}_2$ are the velocities of vortex 1

and 2, respectively, see Figure 2.1b. The initial vortex positions are $\hat{\zeta}_1(0) = \hat{x}_0 + \mathrm{i}(H + \Lambda/2)$ and $\hat{\zeta}_2(0) = \hat{x}_0 + \mathrm{i}(H - \Lambda/2)$, where $H = h_\mathrm{p}/L_0$, and $\hat{x}_0$ is the initial x location.

The vortex sheet has an initial vorticity distribution $\hat{\gamma}(\hat{x}, 0) = 0$, and according to Kelvin's circulation theorem [85], at all subsequent times the vorticity distribution must satisfy

$$\int_{-1}^{1} \hat{\gamma}(\alpha, \hat{t}) \; \mathrm{d}\alpha = 0. \tag{2.5}$$

The boundary conditions on the fluid are that the fluid is at rest with zero pressure at infinity and the velocity component normal to the plate is equal to the plate velocity. The first boundary condition is automatically satisfied by Equation (2.3), while the second boundary condition [73] yields

$$\frac{1}{2\pi} \fint_{-1}^{1} \frac{\hat{\gamma}(\alpha, \hat{t})}{\hat{x} - \alpha} d\alpha = \dot{\hat{\delta}}(\hat{x}, \hat{t}) + \Lambda \Re \left\{ \frac{1}{\hat{x} - \hat{\zeta}_1(\hat{t})} - \frac{1}{\hat{x} - \hat{\zeta}_2(\hat{t})} \right\} \tag{2.6}$$

where $\fint(\cdot)$ is Cauchy's principal value integral and $\Re(\cdot)$ is the real part of the complex variable. The pressure difference induced by the fluid across the plate can be computed using unsteady Bernoulli's equation [86] as

$$[\![\hat{p}]\!](\hat{x}, \hat{t}) = \int_{0}^{\hat{x}} \dot{\hat{\gamma}}(\alpha, \hat{t}) d\alpha + \hat{\gamma}(\hat{x}, \hat{t}) \Re\{\mathrm{Conj}[\hat{w}(\hat{x}, \hat{t})]\}. \tag{2.7}$$

The fluid and structure models are solved simultaneously as outlined by Peterson and Porfiri [73]. Briefly, the plate shape is projected onto a basis set of Chebyshev polynomials, which facilitate solution of Equation (2.6) for the plate vorticity distribution. Combining

21

Equations (2.3) and (2.7), the pressure distribution is then substituted into Equation (2.2) to solve for the plate motion. The vortices are advected via Equation set (2.4). This system of equations is integrated in time to determine the overall system dynamics.

2.2   Vortex ring to vortex pair conversion

Due to the topological differences between a vortex ring, with its looping core, and a two-dimensional vortex pair, with their infinitely long vortex line cores, the velocity and associated pressure fields induced by these fluid structures differ considerably. As such, a vortex ring cannot simply be represented by a vortex pair with identical geometric and kinematic parameters. To encapsulate the salient physics of the fluid-structure interaction, we propose a vortex ring to vortex pair conversion scheme that matches the pressure loading time scale and magnitude on the plate.

The pressure loading time scale is matched between the potential flow model and the experiment by ensuring that the vortex ring and the vortex pair pass the plate at the same rate; that is, the pair and ring must have equal initial convection speed V_c. Note that we are implicitly assuming that the ring and pair convection speeds do not vary significantly during the interaction with the plate, as it is not expected that the influence of the plate on the ring speed would necessarily be the same as that for the vortex pair. Since the convection speeds in both cases are equated, the non-dimensonalization scheme introduced in §2.1 applies to both the ring and the pair, with the plate dynamics parameters μ, β, and η remaining unaltered after the conversion from the experimental configuration to the two-dimensional potential flow representation. With the plate dynamics unaffected by the

conversion, only the vortex pair geometric parameters Λ and H are impacted.

To match the pressure loading magnitude, we first simplify the problem by neglecting the influence of the plate on the fluid. This assumption effectively reduces the matching to a steady state relationship between the pressure distribution at the plane of the undeflected plate in the reference frame of the moving ring/pair. This also neglects the pressure at the back of the plate, which is primarily associated with the plate's movement. Since the plate vibrates in a similar manner as the ring/pair applies similar pressure loading, the differences in the pressure on the back of the plate should be small between the two cases; thus, the pressure loading on the back of the plate may be ignored as a first order approximation. For simplicity, we employ the same coordinate system as depicted in Figure 2.1a at the instant when the vortex ring/pair is passing through the xz-plane.

We begin with a model for an axisymmetric vortex ring with infinitesimal core thickness in an ideal fluid. The axial and radial velocity components $\hat{u}_\mathrm{r}$ and $\hat{v}_\mathrm{r}$ at the plane of the plate ($y = 0$) induced by the ring can be expressed using the Biot-Savart law [87] in dimensionless form as

$$\hat{u}_\mathrm{r}(\hat{x}, \hat{z}) \;=\; \frac{\Lambda_\mathrm{r}\hat{\Gamma}_\mathrm{r}}{8\pi}\left[\left(\frac{\Lambda_\mathrm{r}}{2} + Y\frac{\mathcal{A}}{\mathcal{B}}\right) I_2 - \frac{Y}{\mathcal{B}}I_1\right] \tag{2.8a}$$

$$\hat{v}_\mathrm{r}(\hat{x}, \hat{z}) \;=\; \frac{\Lambda_\mathrm{r}\hat{\Gamma}_\mathrm{r}}{8\pi}\left(\frac{\hat{x}}{\mathcal{B}}\right)(I_1 - \mathcal{A}I_2) \tag{2.8b}$$

23

where

$$Y \;=\; \sqrt{\hat{z}^2 + H_{\mathrm{r}}^2} \tag{2.8c}$$

$$\mathcal{A} \;=\; \hat{x}^2 + Y^2 + \Lambda_{\mathrm{r}}^2/4 \tag{2.8d}$$

$$\mathcal{B} \;=\; -\Lambda_{\mathrm{r}}Y \tag{2.8e}$$

$$\mathcal{C} \;=\; \sqrt{\hat{x}^2 + (Y + \Lambda_{\mathrm{r}}/2)^2} \tag{2.8f}$$

$$\lambda \;=\; 2\Lambda_{\mathrm{r}}Y/\mathcal{C}^2 \tag{2.8g}$$

$$I_1 \;=\; \frac{4}{\mathcal{C}}\mathcal{K}(\lambda) \tag{2.8h}$$

$$I_2 \;=\; \frac{4}{\mathcal{C}^3}\frac{\mathcal{E}(\lambda)}{1 - \lambda} \tag{2.8i}$$

and $\hat{\Gamma}_{\mathrm{r}} = \Gamma_{\mathrm{r}}/V_0 L_0$ is the dimensionless circulation for the vortex ring. $\mathcal{K}(\lambda)$ and $\mathcal{E}(\lambda)$ represent complete elliptic integrals of the first and second kind, respectively. Similarly, to obtain the steady state Cartesian velocity components $\hat{u}_{\mathrm{p}}$ and $\hat{v}_{\mathrm{p}}$ at the plane of the plate for an analogous vortex pair, we rewrite Equation (2.3), without the vortex sheet, as

$$\hat{u}_{\mathrm{p}}(\hat{x}) \;=\; \Lambda_{\mathrm{p}}\left[\frac{\Lambda_{\mathrm{p}}/2 - H_{\mathrm{p}}}{\hat{x}^2 + (\Lambda_{\mathrm{p}}/2 - H_{\mathrm{p}})^2} + \frac{\Lambda_{\mathrm{p}}/2 + H_{\mathrm{p}}}{(\hat{x}^2 + \Lambda_{\mathrm{p}}/2 + H_{\mathrm{p}})^2}\right] \tag{2.9a}$$

$$\hat{v}_{\mathrm{p}}(\hat{x}) \;=\; \Lambda_{\mathrm{p}}\left[\frac{\hat{x}}{\hat{x}^2 + (\Lambda_{\mathrm{p}}/2 - H_{\mathrm{p}})^2} - \frac{\hat{x}}{\hat{x}^2 + (\Lambda_{\mathrm{p}}/2 + H_{\mathrm{p}})^2}\right] \tag{2.9b}$$

We note that while $\hat{u}_{\mathrm{r}}$ and $\hat{v}_{\mathrm{r}}$ correspond to cylindrical velocity components of the ring (azimuthal and radial components, respectively) and $\hat{u}_{\mathrm{p}}$ and $\hat{v}_{\mathrm{p}}$ are Cartesian velocity components of the pair (in the x and y directions, respectively), the components are aligned when $z = 0$, corresponding to the centerline of the plate. In what follows, we often refer

to these components as $\hat{u}$ and $\hat{v}$ for both models.

The pressure field at the plane of the plate due to the vortex ring $\hat{p}_{\mathrm{r}}(\hat{x}, \hat{z})$ and pair $\hat{p}_{\mathrm{p}}(\hat{x})$ can be obtained from the steady state Bernoulli's equation,

$$\hat{p}_{\mathrm{r}}(\hat{x}, \hat{z}) = -\frac{1}{2}\left[\hat{u}_{\mathrm{r}}^2(\hat{x}, \hat{z}) + \hat{v}_{\mathrm{r}}^2(\hat{x}, \hat{z})\right] \tag{2.10a}$$

$$\hat{p}_{\mathrm{p}}(\hat{x}) = -\frac{1}{2}\left[\hat{u}_{\mathrm{p}}^2(\hat{x}) + \hat{v}_{\mathrm{p}}^2(\hat{x})\right] \tag{2.10b}$$

Note that in obtaining Equation (2.10) we have assumed that the pressure and velocity of the fluid both vanish to zero in the far field. An exact match of the pressure profile is not expected; however, we find that the pressure profiles at the plane of the plate (along the x axis) have similar bell curve-like profiles for both the ring and the pair, which enables the determination of an optimal match by requiring the two profiles to have equal peak and integrated values along the plane the plate.

To match the peak pressure value, which occurs directly beneath the ring/pair at $\hat{x} = 0$, we set

$$\hat{p}_{\mathrm{p}}(0) - \frac{2}{\hat{W}} \int_0^{\hat{W}/2} \hat{p}_{\mathrm{r}}(0, \hat{z}) \, \mathrm{d}\hat{z} = 0 \tag{2.11}$$

where $\hat{W} = W/L_0$. The integral is the average pressure across the width of the plate, which accounts for variations in the pressure due to the vortex ring curvature in the $\hat{z}$ direction, see Figure 2.1a. By noting that only the $\hat{u}$ component of the velocity exists at $\hat{x} = 0$ for both the ring and the pair, substitution of Equations (2.9a) and (2.8a) into

25

Equation (2.10), and subsequent substitution into Equation (2.11) yields

$$H_{\mathrm{p}} = \left(\frac{1}{4} - \frac{1}{U} \right)^{\frac{1}{2}} \Lambda_{\mathrm{p}} \qquad (2.12a)$$

where

$$U = \frac{2}{\hat{W}} \int_{0}^{\hat{W}/2} \hat{u}_{\mathrm{r}}(0, \hat{z}) \; \mathrm{d}\hat{z}. \qquad (2.12b)$$

Equation (2.12) provides a relationship between the vortex pair geometric parameters (spacing between the vortices, Λ_{p}, and distance of the pair from the plate, H_{p}) and the vortex ring parameters, which are encapsulated in U.

An additional relationship is required to solve for Λ_{p} and H_{p} in terms of the vortex ring parameters. This is accomplished by matching the force induced by the ring and the pair at the plane containing the plate. Equating the integrated pressure for the ring and the pair yields

$$\int_{0}^{\infty} \hat{u}_{\mathrm{p}}^{2}(\hat{x}) + \hat{v}_{\mathrm{p}}^{2}(\hat{x}) \; \mathrm{d}\hat{x} - F = 0 \qquad (2.13a)$$

where

$$F = \frac{2}{\hat{W}} \int_{0}^{\hat{W}/2} \int_{0}^{\infty} \hat{u}_{\mathrm{r}}^{2}(\hat{x}, \hat{z}) + \hat{v}_{\mathrm{r}}^{2}(\hat{x}, \hat{z}) \; \mathrm{d}\hat{x} \; \mathrm{d}\hat{z} \qquad (2.13b)$$

The bounds of the integrals above are from $\hat{x} = 0$ to $\hat{x} = \infty$ since the pressure profile is symmetric about the xy-plane.

Equations (2.12) and (2.13) can be solved simultaneously for the two unknown vortex pair parameters Λ_{p} and H_{p}. We note that the vortex pair circulation Γ_{p} is a dependent parameters since it can be computed from the known vortex pair convection speed and pair

26

geometry, as discussed previously. The vortex pair parameters Λ_p and H_p can be obtained by first calculating the vortex ring constants U and F, then substituting Equation (2.12) into Equation (2.13) to yield Λ_p. Finally, H_p can be found directly from Equation (2.12). The solution procedure enables efficient estimation of the vortex pair parameters that best match the pressure distributions for a given vortex ring/plate configuration without the need to apply a more computationally expensive optimization procedure to minimize the error between the vortex ring and the vortex pair pressure profiles at each point.

An example of the output of this conversion method is shown in Figure 2.2, which compares the pressure and the velocity components at the plate centerline (x-axis) of a vortex ring and its matched two-dimensional vortex pair for a plate of zero width ($\hat{W} = 0$). In this case, the integrals in Equations (2.11) through (2.13) with respect to $\hat{z}$ are replaced by their integrands, that is, there is no averaging across the plate width. From Figure 2.2a, we see that the vortex pair pressure profile is nearly identical to that of the vortex ring after matching. However, owing to the distinctly different topology of the vortex filaments in the ring and pair cases, there are small differences in the individual velocity components, as shown in Figure 2.2b and 2.2c. These differences in the velocity components in the two cases can potentially lead to some error once the influence of the plate is included. For finite width plates $\hat{W} > 0$, the matched vortex pair pressure profile tends to under-predict the pressure near the centerline of the plate and over-predict the values nearer the edges of the plate due to the averaging effect. Overall, the matching enables representation of a vortex ring by a two-dimensional pair with nearly identical pressure loading distributions on a plate in the fluid, as well as identical interaction time scales due to matching the convection speeds of the ring and pair.
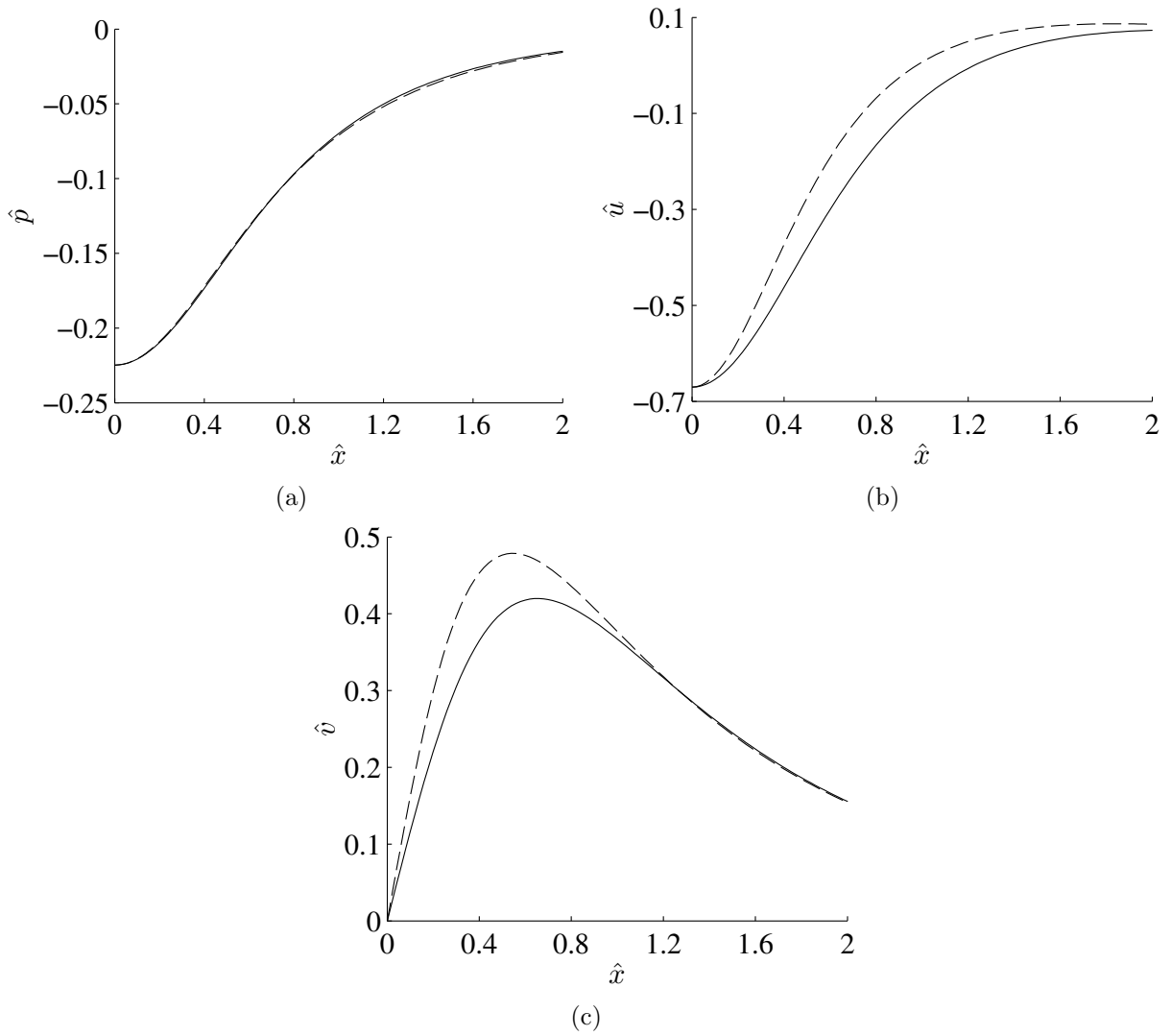
Figure 2.2: Comparison of the (a) pressure, (b) $\hat{u}$ velocity, and (c) $\hat{v}$ velocity profiles between a vortex ring and its matched vortex pair for a plate of zero width. Solid lines and dash lines represent the vortex pair and the vortex ring, respectively.

2.3 Model Validation

To validate the analytical solution, model predictions are compared with the experimental results of Goushcha *et al.* [76]. Their experimental campaign employed a polycarbonate strip of dimensions $L = 0.1$ m, $W = 0.03$ m, and $T = 0.05$ mm. Reported vortex ring parameters are $\Gamma_r = 0.77$ m^2/s and $V_c = 2.81$ m/s. Additionally, the ring diameter $a_r = 0.14$ m and distance of the ring from the plate $h_r = 0.096$ m used in their study were obtained through personal communication [88]. The value of h_r used in the analytical solution was slightly modified to $h_r = 0.1011$ m to better match the reported pressure loading on the plate. This modest adjustment is, however, within the uncertainty limits of the experiments.

In addition to the plate geometry and vortex ring parameters, Goushcha *et al.* reported the first mode natural frequency to be 48.3 rad/s. They further presented a time series of the measured strain at the clamped end of the plate in their Figure 3. Estimating the plate natural frequency from this time series yields a value of $40.0\,$rad/s, which is within 20% of their reported value. Hypothesizing that the mass density per unit volume of the polycarbonate is $\varrho = 1200$ kg/m^3 [89–93], matching the fundamental resonance frequency to the reported value yields an effective Young's modulus $\Upsilon = 109$ GPa. Such an estimate of the Young's modulus is outside the range typical of polycarbonate which is between 2.35 and 2.4 GPa [89–93]. It is tenable to hypothesize that the thickness was higher than the reported value, which we thus change to $T = 0.3$ mm to set the effective Young's modulus at $\Upsilon = 2.4\,$GPa. We note that other possible contributors the discrepancy include the impact of the strain gauge on the material stiffness and/or free vibration length,

or incorrect material properties. A detailed study determined that these influences were relatively small. The damping factor C is selected to match the decay rate of the free vibration presented in their Figure 3.

The dimensionless parameters used for the analytical solution are $\beta = 4.466$, $\mu = 5.878$, $\eta = 0.419$, $\Lambda = 1.004$, and $H = 1.335$; the latter two parameters were obtained using the conversion method discussed in §2.2. We only employ the first in-vaccuum mode of the plate to simulate the plate dynamics in the analytical solution. This is in agreement with the experimental observations of Goushcha *et al.* that the plate vibrates along its fundamental mode shape. Including additional modes in the analysis does not significantly affect the results.

Figure 2.3 presents details of the vortex pair/plate interaction predicted from the analytical model based upon the experimentally-derived governing dimensionless parameters. The left-most column shows the positions of the vortex pair (circles) and the plate (solid line), with the trajectories of the vortices depicted by dashed lines. The middle column shows the corresponding plate deflection, while the right column shows the differential pressure loading on the plate. Time is increasing from one row to the next. As the vortices approach the plate from the right, there is a positive pressure jump across the plate, that is, the pressure on the top of the plate is higher, which causes a negative plate deflection (row 1). As the vortices pass above the plate, a strong negative pressure on the plate develops due to the low pressure vortex core, which pulls on the plate (rows 2-4). In turn, the plate motion influences the trajectory of the vortex pair, drawing the pair in the negative $\hat{y}$ direction. Once the vortex pair passes beyond the plate, there is again a positive pressure loading on the plate (row 5). We note that due to the inertia of the plate, its deflection is

30
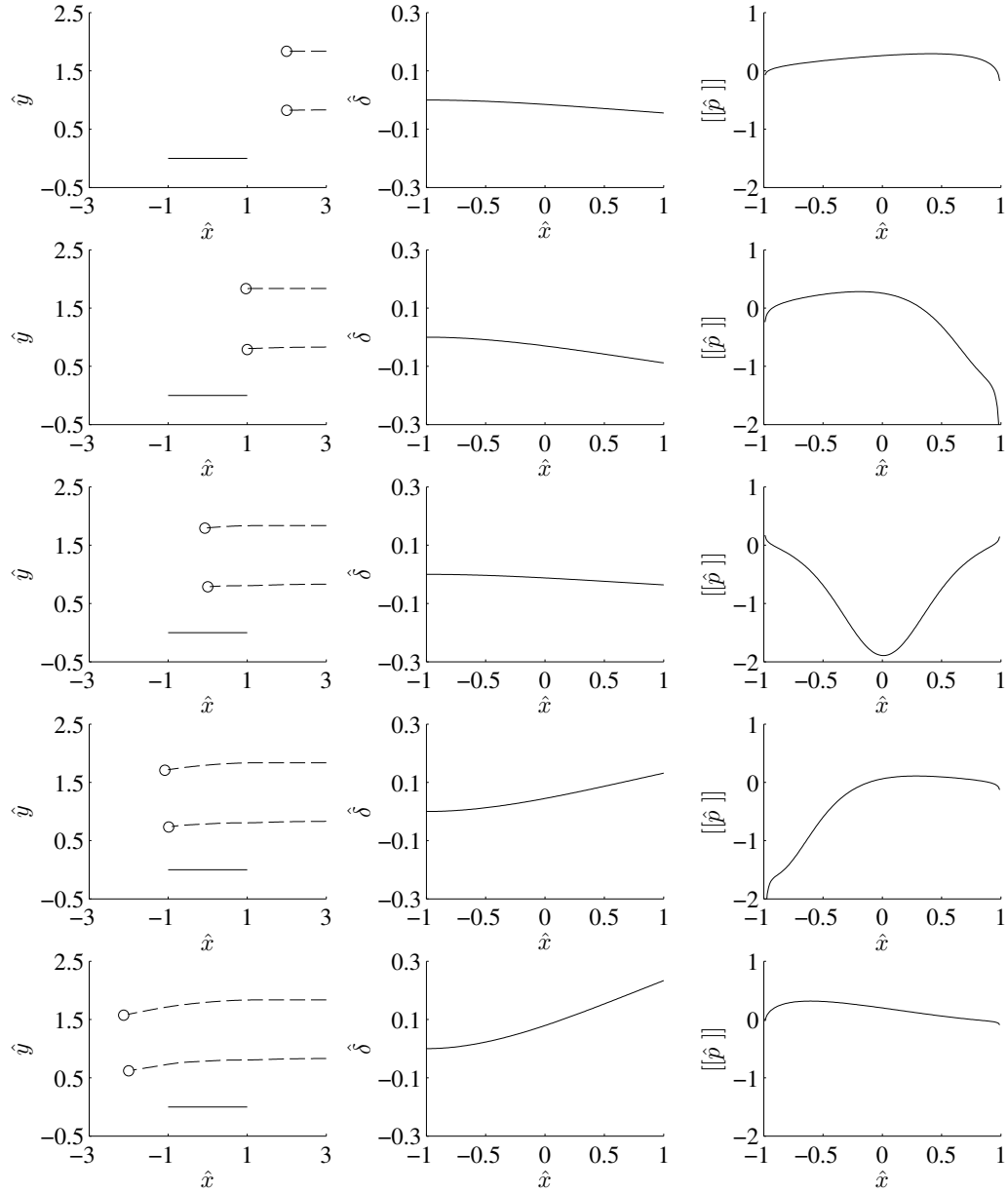
Figure 2.3: Snapshots of the vortex pair/deformable plate interaction. The left column displays the position (circles) and the trajectories (dashed lines) of the vortices with respect to the plate (solid lines). The middle column displays the plate deflection, while the right column shows the pressure jump across the plate. Row 1: $\hat{t} = 9.02$; row 2: $\hat{t} = 10.08$; row 3: $\hat{t} = 11.15$; row 4: $\hat{t} = 12.16$; and row 5: $\hat{t} = 13.20$.

31

not necessarily in phase with the pressure loading. This process qualitatively agrees with the experimental observations of Goushcha *et al* and a similar positive pressure jump is observed for a vortex advecting past a structure in a free stream [94].

A more quantitative validation of the model is presented in Figure 2.4, which compares the plate tip deflection $\hat{\delta}(1, \hat{t})$, the pressure loading on the plate $[\![\hat{p}]\!]$ when the vortex ring/pair is positioned at $\hat{x} \approx -0.04$, and the net force per unit width $\hat{f}$ as a function of vortex ring/pair position between the analytical solution and the experimental data. The experimental data for the tip deflection shown in Figure 2.4a were not published in the original experimental paper, but were provided through personal communication and are reproduced herein with permission [88]. The integrated force per unit width in Figure 2.4c is computed as

$$\hat{f}(\hat{t}) = - \int\limits_{-1}^{1} [\![\hat{p}]\!](\hat{x}, \hat{t}) \, \mathrm{d}\hat{x}. \tag{2.14}$$

with $\hat{t}$ as a function of $\Re\{\hat{\zeta}_2\}$.

The deflection (Figure 2.4a) shows generally good agreement between the present analytical solution and the experimental data. The analytical solution under-predicts the first positive peak in both cases by $\approx 20\%$, though subsequent positive peaks match very well.

The pressure distribution on the plate when the vortex ring/pair is located over the center of the plate is presented in Figure 2.4b for both the experimental data, obtained using PIV, and the analytical prediction. The minimum pressure across the plate is located at approximately the same $\hat{x}$ position as the vortex ring/pair, which corresponds to $\hat{t} \approx 11$ in Figures 2.4a. The minimum pressure peak is matched in both magnitude and location between the experiment and the model, though the overall pressure distribution is slightly

32
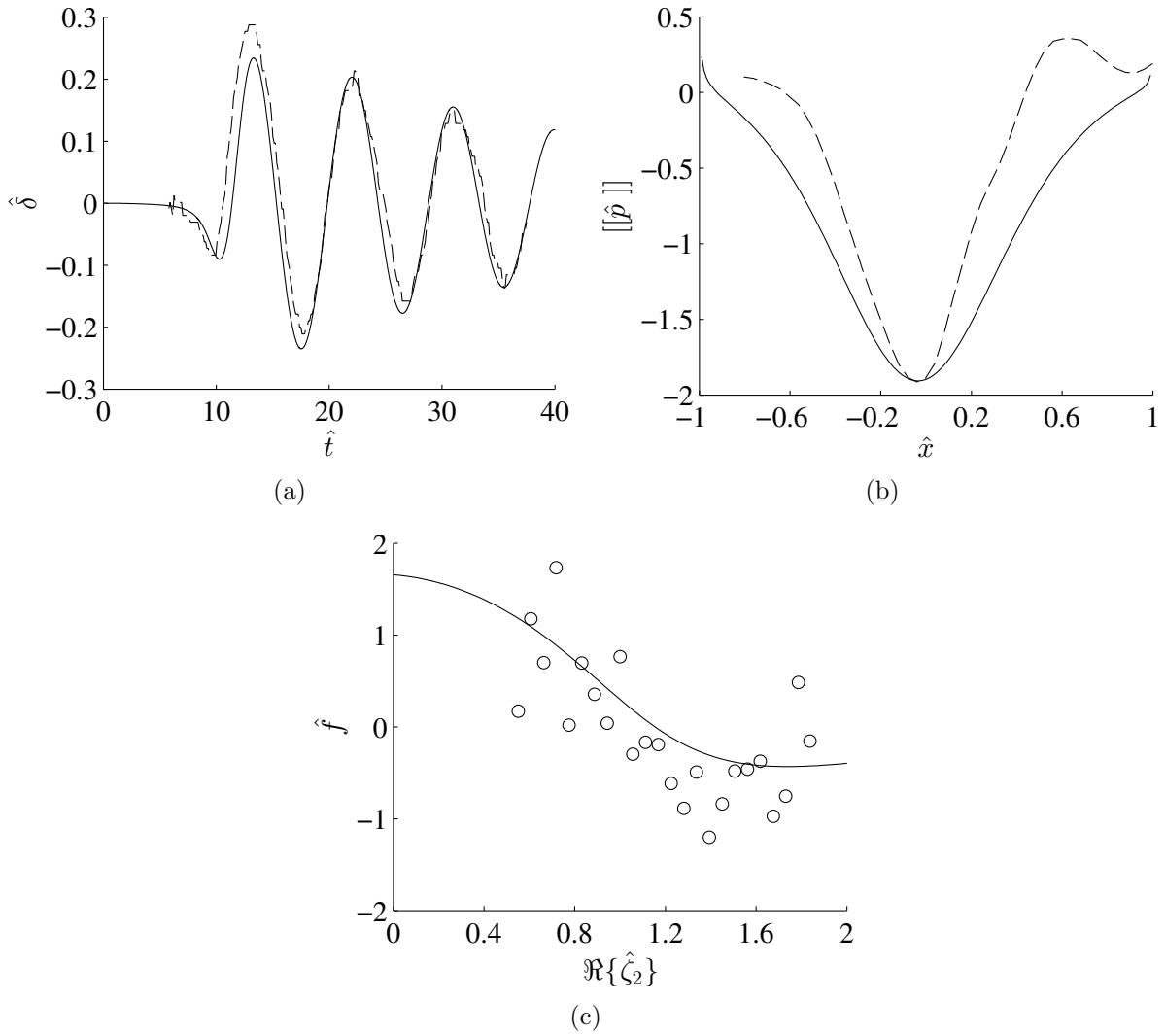
Figure 2.4: Comparison between model predictions and experimental measurements of (a) the plate tip deflection, (b) the differential pressure loading on the plate when the vortex ring/pair is located at $\hat{x} \approx -0.04$, and (c) integrated force per unit width on the plate versus position of the bottom vortex $\Re\{\hat{\zeta}_2\}$. The analytical results are represented by solid lines. The experimental data are depicted by a dashed line in (a), and circles in (b) and (c).

wider for the model prediction. In addition, experimental data have a relatively pronounced positive peak in the pressure near the free end of the plate that is not captured by the potential flow solution.

The integrated force on the plate is plotted as a function of bottom vortex position $\Re\{\hat{\zeta}_2\}$ (see Figure 2.1b) in Figure 2.4c. Note, for the experimental data, "bottom vortex position" refers to the x position of the portion of the vortex ring core that is closest to the plate, see for example Figure 3 of Goushcha *et al.* In Figure 2.4c, the experimental data, again obtained from PIV, are noisy, but agree well with the model prediction in terms of trend and magnitude.
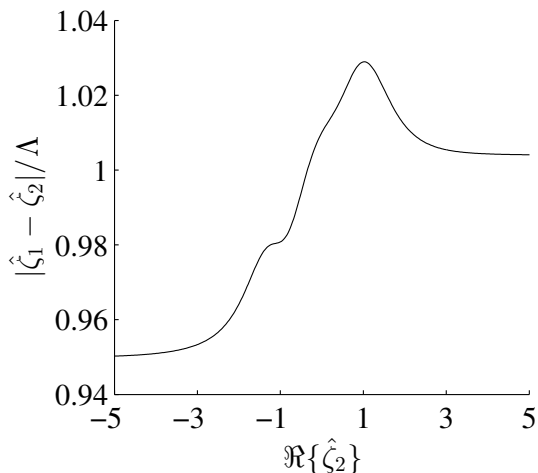
Figure 2.5: Change of vortices separation distance with respect to its initial condition Λ as a function of the bottom vortex location $\Re\{\hat{\zeta}_2\}$.

The conversion procedure from vortex ring properties to a representative vortex pair implicitly assumes that the vortex ring/pair convection speed is not significantly influenced by the presence of the plate, as discussed in §2.2. We observe in Figure 2.3 that the trajectories of the vortices constituting the vortex pair are modestly influenced by the

plate. Given that the vortices have constant circulation, a relative change in trajectory of one vortex in the pair with respect to the other can result in an altered convection speed of the pair; that is, if the vortices move closer to one another their mutual induction speed will increase, for example. Figure 2.5 plots the distance between the vortices in the pair normalized by their initial separation, $|\hat{\zeta}_1 - \hat{\zeta}_2|/\Lambda$, as a function of the position of the bottom vortex, $\Re\{\hat{\zeta}_2\}$, as it passes over the plate. As the vortex pair approaches the plate, $\Re\{\hat{\zeta}_2\}$ decreases from the initial value of x_0, and the vortices begin to move apart slightly, indicating that the convection speed decreases. Once the pair reaches the free end of the plate ($\Re\{\hat{\zeta}_2\} = 1$), the vortices start to move closer together as they are deflected downwards due to the interaction with the plate; see also the first column in Figure 2.3. The vortices continue to move closer together after advecting past the plate before stabilizing into a new configuration with a final separation distance that is 5% closer than their initial separation (V_c is increased by 5%). Over the course of the interaction, changes in the convection speed of the pair are very modest, as originally assumed for the vortex ring to pair conversion.

As a final note on the applicability of the potential flow model, the ideal fluid assumption neglects vorticity generation, dissipation, and shedding along the plate [95]. These viscous effects will introduce additional hydrodynamic loading onto the plate which the potential model does not capture [14,96–99], as well as a train of wake vortices convecting away from the tip of the plate [95, 100]. Based upon the agreement between experimental data and model prediction presented above, these viscous effects are expected to play a secondary role for a vortex pair sufficiently far from the plate during the initial interaction stage. Viscous effects are partially accounted for by the structural damping coefficient η, which is identified
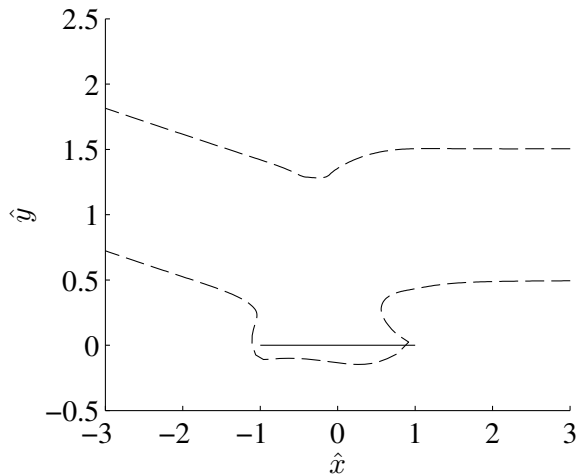
35

Figure 2.6: Non-physical behavior of a vortex pair/plate interaction in an ideal fluid, wherein the bottom vortex is "trapped" by the plate. In this case, vorticity interaction between the plate and vortex pair would be non-negligible.

in in-air experiments rather than trials in-vacuum. As a result, η likely over-predicts the inherent structural damping, compensating for some of the unmodelled viscous effects. However, if the initial vortex pair positions and trajectory result in the pair coming too close to the plate, then non-physical vortex trajectories can occur, as shown in Figure 2.6. In this case, the trajectory of vortex 2 is significantly altered, with the vortex actually passing around the bottom side of the plate before joining with vortex 1 again and advecting away from the plate. The proximity of vortex 2 to the plate would, in fact, lead to non-negligible viscous effects, namely, vorticity generation along the plate and subsequent interaction with the pair vorticity [69, 74]. Thus, the potential flow model behavior should be expected to deviate considerably from experimental observations of real fluids. For the remainder of the document we restrict ourselves to cases in which viscous effects are small and the potential flow model as described in §2.1 is reasonable. Lastly, we call attention to the fact that the

36

matching method is only valid for cases where the width is small compared to the vortex ring radius a_{r} and the vortex ring to plate distance H_{r}.

2.4　Energy Transfer Optimization

With the analytical model for the energy harvesting configuration shown in Figure 2.1a validated against the experimental data of Goushcha *et al.*, we now focus on employing the model to optimize the energy exchange between the vortex structure and the plate; that is, we aim to optimize the plate properties for a given set of vortex parameters in order to maximize the energy transferred to the plate. We note that energy harvesting can be estimated through the addition of a damping term in the governing equations; however, we are principally concerned with the total energy transferred from the fluid to the plate, as the fluid is the sole energy source in this interaction. Details of the energy transduction through electromechanical coupling, which is material dependent, is not considered. In this case, we consider maximizing the total energy transferred from the fluid to the plate as maximizing the total mechanical energy that is available for electrical conversion, which in terms maximizing the energy harvesting potential. This assumes, of course, weal electromechanical coupling. The nondimensional energy of the plate, $\hat{E}$, is given by [73],

$$\hat{E}(\hat{t}) = \frac{1}{2} \int\limits_{-1}^{1} \mu \left[\dot{\hat{\delta}}(\hat{x}, \hat{t}) \right]^2 + \beta \left[\hat{\delta}^{\mathrm{II}}(\hat{x}, \hat{t}) \right]^2 \, \mathrm{d}\hat{x} \tag{2.15}$$

where $\hat{E} = E / \rho V_0^2 L_0^2$. The first term in Equation (2.15) corresponds to the plate kinetic energy and the second term represents the material strain potential energy. Both terms

37

comprise a non-dimensional parameter that is a function of the physical properties of the plate coupled with the dynamic response of the plate. Note that for the energy transfer optimization, we neglect damping ($\eta = 0$), which, in turn, neglects all losses in the system in order to facilitate comparisons of the total plate energy acquired from the vortex pair. This assumes that viscosity does not play a significant role in the initial vortex pair-plate interaction, which was demonstrated in the previous section, and that structural damping is relatively weak.
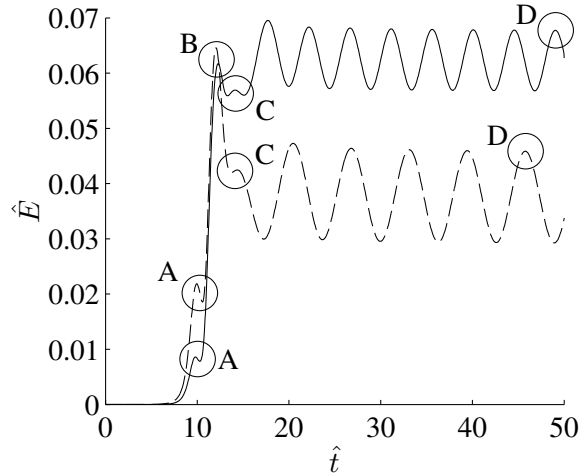
Figure 2.7: The energy of the plate as a function of time; the solid line represents dimensionless parameters matching the experiments of Goushcha *et al.* ($\mu = 5.878$, $\beta = 4.466$, $H = 1.335$, $\Lambda = 1.004$, $\eta = 0$); the dashed line represents an alternative parameter set with lower mass and stiffness ratios ($\mu = 2.000$, $\beta = 1.000$, $H = 1.335$, $\Lambda = 1.004$, $\eta = 0$).

The total plate energy as a function of time for two different plate/vortex pair parameter sets is presented in Figure 2.7. The solid line corresponds to the parameters representative of the experiments of Goushcha *et al.* in the absence of damping ($\mu = 5.878$, $\beta = 4.466$, $H = 1.335$, $\Lambda = 1.004$, and $\eta = 0$), while the dashed line has lower mass and stiffness ratios ($\mu = 2.000$ and $\beta = 1.000$). In both cases, as the pair approaches the plate it deflects,

38

resulting in an increase in the total plate energy. The plate then reaches a local maximum in energy, denoted as point A in Figure 2.7, when the vortex pair is near the free end of the plate. After point A, the plate energy decreases slightly before rapidly rising to point B as the vortex pair passes over the plate. Once the pair passes beyond the plate there is again a drop in energy to point C, after which the plate settles into a free vibration state, which is evident in the the harmonic oscillation in the plate energy after point C. We note that the harmonic oscillation in the plate energy during free vibration is due to the exchange between the kinetic energy of the vortex sheet [85] and the total energy of the plate via fluid-structural coupling. Shvydkoy [101] demonstrated that a vortex sheet with zero total circulation has finite energy, which is conserved in the absence of the interactions; this condition is automatically satisfied for all time in the present model in Equation (2.5) and, therefore, the vortex sheet simply acts as another energy storage element in the system during steady state free vibration.

As mentioned previously, the total energy available for harvesting is related to the total plate energy. As shown in Figure 2.7, the plate energy never settles to a fixed value, making assessment of the total energy transferred somewhat nebulous. Herein, we define the "steady state" plate energy $\hat{E}_{\text{ss}}$ as the peak energy of the plate during the free vibration of the plate once the vortex pair has advected away; this point is denoted as D in Figure 2.7. Point D does not necessarily correspond to the maximum energy achieved by the plate due to the interaction with the vortex pair; in fact, point B is considerably larger than point D for the dashed line in Figure 2.7. However, the energy in the plate is quickly transferred back to the fluid in this case, with the free vibration phase having considerably less total energy than at point B. For the solid line, corresponding to the experimental conditions of

39

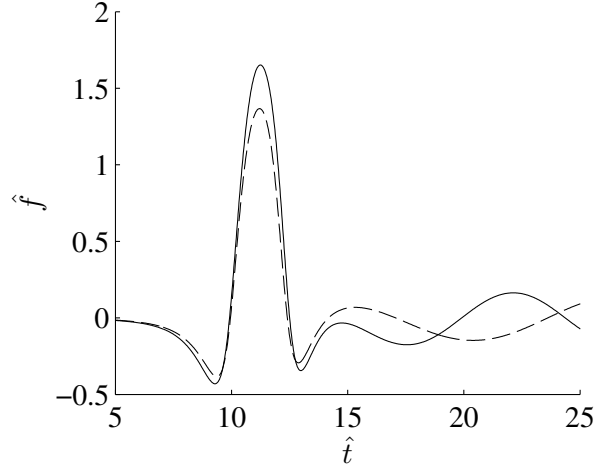Goushcha *et al.*, point D is near the maximum energy obtained by the plate.

Figure 2.8: Integrated force on the plate with respect to time; the solid line represents dimensionless parameters matching the experiments of Goushcha *et al.* ($\mu = 5.878$, $\beta = 4.466$, $H = 1.335$, $\Lambda = 1.004$, and $\eta = 0$); the dashed line represents an alternative parameter set with lower mass and stiffness ratios ($\mu = 2.000$, $\beta = 1.000$, $H = 1.335$, $\Lambda = 1.004$, and $\eta = 0$).

Though qualitatively similar in behavior, there are significant differences in the plate energy at the highlighted points in Figure 2.7 for the two cases; a 66% reduction in μ and 78% reduction in β results in a 154% increase at point A, a 4.7% increase at point B, a 25% reduction at point C, and a 32% reduction in $\hat{E}_{\mathrm{ss}}$ (point D). To further elucidate the physics associated with this behavior, we consider the integrated loading on the plate. Figure 2.8 shows the integrated force along the plate as a function of time, computed using Equation (2.14), for the two parameters sets presented in Figure 2.7. As the vortex pair approaches the plate, there is a negative force on the plate that increases in magnitude as the distance of the pair from the plate free end decreases ($\hat{t} <\sim 10$). As the vortices pass over the plate ($\sim 10 < \hat{t} <\sim 12.5$), there is a strong positive force due to the low pressures

40

of the vortex cores pulling the plate towards the pair. The force again goes negative once the vortices are beyond the plate ($\sim 12.5 < \hat{t} <\sim 14$). Oscillations in the force on the plate after the interaction $\hat{t} >\sim 15$ are due primarily to the plate free vibration. We note that in the free vibration phase, the plate energy oscillates at twice the frequency of the forcing, since maximum energy is achieved twice per period.

As evidenced by Figure 2.8, there is an inherent time scale to the vortex pair/plate interaction, which is a function of the vortex parameters H and Λ. In both cases shown in the figure, the vortex pair positions and parameters are identical, and as such, the time scale of the interaction, denoted by the negative-positive-negative peaks around $9 < \hat{t} < 13$, are the same. There is a difference in the loading magnitude between the two cases, however, due to the differing degrees of coupling between the fluid and the structure associated with the differing mass and stiffness ratios. Specifically, for the dashed line, the mass and stiffness ratio are smaller than for the solid line, and thus the plate more readily deflects due to the incoming vortex pair, resulting in a lower peak loading. The plate natural frequency for the two cases differ, resulting in divergence of the loading in the free vibration phase ($\hat{t} >\sim 15$).

Figure 2.8 suggests a manner in which the plate dynamics may be optimized for energy transferring; specifically, resonance will occur if the characteristic frequency of the pressure loading matches the plate natural frequency. This will, in turn, lead to larger plate deflection and an increase in the energy transfer capacity. Out of phase loading, however, results in the plate energy returning back to the fluid after the vortex interaction, as seen in point C of the dashed line in Figure 2.7. This is analogous to the frequency response of a single degree of freedom system [102].

To more clearly illustrate the coupling between the vortex pair convection and the plate response, a simplified analysis can be performed by representing the pressure loading of the vortex pair with a traveling point load with time-varying magnitude to mimic the negative-positive-negative loading observed during the interaction in Figure 2.8. In this case, the loading term in Equation (2.1) is

$$- \llbracket p \rrbracket (x, t) = P_0 \ \sin(\omega_\mathrm{P} t) \ \delta_\mathrm{D}(x - x_0 + V_\mathrm{c} t) \tag{2.16}$$

where δ_D is the Dirac delta distribution. The point load is travelling at a constant velocity V_c, and has a harmonic magnitude with a frequency of ω_P. We note that ω_P represents the characteristic frequency of the pressure loading in this simplified analysis, which is a function of the advective time scale. Fryba [103] demonstrated that in this simplified scenario, resonance occurs when

$$\omega_\mathrm{i}^\mathrm{res} = \omega_\mathrm{P} \pm (\lambda_i L) \frac{V_\mathrm{c}}{L} \tag{2.17}$$

where ω_i and $(\lambda_i L)$ are the natural frequency and the characteristic constant for each mode, respectively. The simplified model neglects the loading distribution along the x-axis and the fluid-structure coupling, but it does highlight the important relationship between the vortex pair convection speed and the characteristic frequency of the loading, since both terms in Equation (2.17) are functions of V_c. We note that even when the point load has a constant magnitude, the resonance still occurs when $\omega_\mathrm{i}^\mathrm{res} = V_\mathrm{c}/L$, see Ref. [103].

Based upon the above discussion, it is evident that the convection speed is key to

achieve resonance; thus, we seek the appropriate plate natural frequency to loading time scale ratio that maximize the steady state energy, E_{ss}. Using the nondimensionalization scheme discussed in §2.1, the dimensionless natural radian frequency of the first plate vibration mode is defined as

$$\Omega_1 = 2\frac{\omega_1 L}{V_c(\lambda_1 L)^2} = \sqrt{\frac{\beta}{\mu}}. \tag{2.18}$$

where ω_1 is the plate fundamental natural radian frequency and $\lambda_1 = 1.8751/L$ is the corresponding eigenvalue. To investigate the optimal plate/vortex pair parameters in terms of energy transfer to the plate, we parametrically vary Ω_1 and μ and evaluate the steady state plate energy $\hat{E}_{\text{ss}}$. Figure 2.9a plots E_{ss} as a function of Ω_1 and μ for the experimental configuration of Goushcha *et al.* in the absence in damping, that is $H = 1.335$, $\Lambda = 1.004$, and $\eta = 0$.

It is clear from the parametric study result in Figure 2.9a that there is an optimal dimensionless natural frequency that maximizes $\hat{E}_{\text{ss}}$ at a given value of μ, which is indicated by the dashed line. This dashed line corresponds to the resonance condition alluded to in Equation (2.17), which results in a significant boost to the steady state plate energy. The resonance condition occurs at the frequency of $\Omega_1^{\text{res}} \approx 2.02$ for $\mu = 1$, and decreases as μ increases. The rate of change in Ω_1^{res} decreases as μ increases, suggesting that the coupling effect decreases as the mass ratio increases, which is in agreement with the study by Peterson and Porfiri [73] for a vortex pair orthogonally approaching and passing around a deformable plate. Additionally, there is an overall increase in E_{ss} as μ decreases, which suggests that one can improve the energy transferring by reducing the plate mass or, more practically, adjusting its thickness. However, one should be aware that the bending
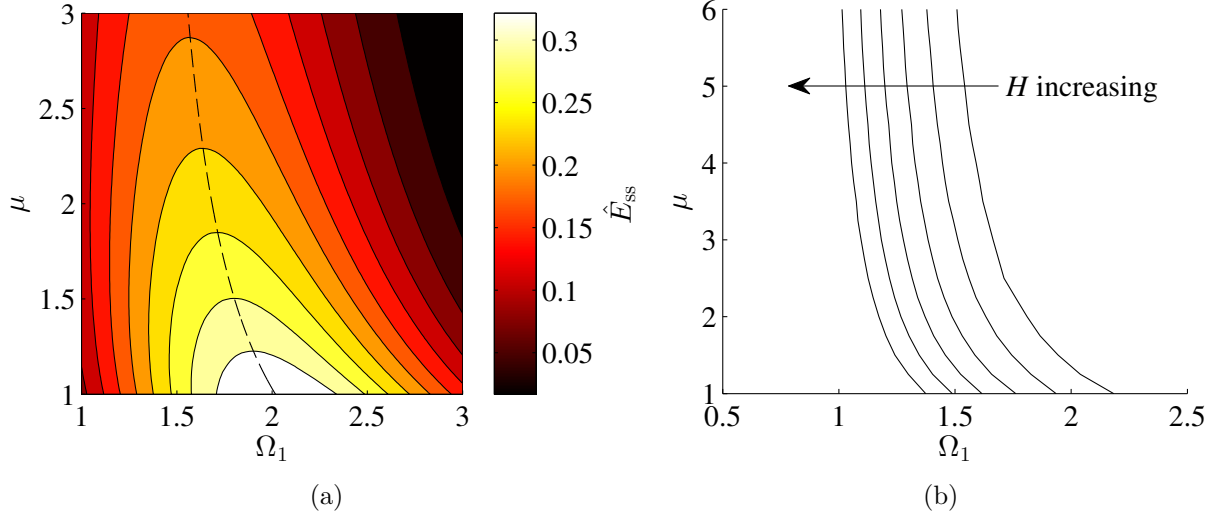
Figure 2.9: (a) Parametric study of the steady state plate energy $\hat{E}_{ss}$ for the experimental vortex pair parameters $H = 1.335$ and $\Lambda = 1.004$ with zero damping $\eta = 0$; the dashed line indicates the resonant frequency. (b) Parametric study of the resonance frequency Ω_1^{res} with respect to changes in H. Solid lines indicated where $\hat{E}_{ss}$ is maximized for H ranging from 1.2 to 2.2 with $\Lambda = 1.004$ and $\eta = 0$.

stiffness is sensitive to the plate thickness as well, which impacts the dimensionless natural frequency.

Figure 2.9a focuses on optimizing the plate parameters for the experimental geometry described by Goushcha *et al.*, which has a fixed vortex ring height above the plate. That is, for a given vortex ring/plate configuration, Figure 2.9a provides insight into the best μ and Ω_1 for maximum energy transfer to the plate. In terms of pressure loading on the plate, the closer the vortex ring/pair passes by the plate, the larger the pressure loading magnitude, and consequently the larger the plate deflection. Thus, it is important to examine how the resonance frequencies vary with changing H. We note that by changing H for the

vortex pair, the corresponding vortex ring parameters change as well due to the conversion described in §2.2. Figure 2.9b presents the shift in the resonance peaks for H ranging from 1.2 to $H = 2.2$ with $\Lambda = 1.004$ and $\eta = 0$. As H increases, the dimensionless resonance frequency shifts towards lower values. In addition, the resonant frequencies are a weaker function of μ for larger values of H, demonstrating that coupling decreases as the pair is further away from the plate.
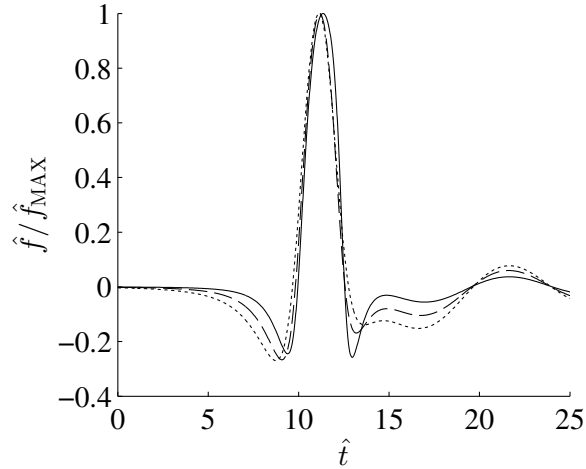
Figure 2.10: Integrated force on the plate normalized by its maximum value with respect to time with $H = 1.2$, $H = 1.6$, and $H = 2.0$ represented by solid, long dashed, and short dashed lines respectively. ($\mu = 5.878$, $\beta = 4.466$, $\Lambda = 1.004$, and $\eta = 0$)

To understand the shift in resonance frequency as H changes, we compare the force loading on the plate at $H = 1.2$, $H = 1.6$ and $H = 2.0$ in Figure 2.10. In order to observe the differences in the loading characteristic frequency, the force is normalized by its max value for direct comparison. As shown in Figure 2.10, the primary positive peaks have similar profiles at different H, but the negative peaks vary noticeably. The first negative peak becomes wider and has a small increase in the relative magnitude in comparison to

the primary positive peak as H increases, while the second negative peak becomes much weaker. The significant drop in the relative magnitude of the second negative peak as H increases is due to the fluid-structure coupling reduction, which results in a smaller vortex pair path deflection towards the plate and leads to a drop in relative forcing.

To aid in energy harvester selection, we present the dimensionless plate bending stiffness β that results in resonance for a given dimensionless plate mass μ and dimensionless vortex pair height above the plate H. This is obtained by fitting the parametric study results in Figure 2.9b, yielding

$$\beta = 4.264\mu e^{-0.7314H} + 4.072H^{-1.737} \tag{2.19a}$$

The coefficient of determination is $R^2 = 0.9998$ for Equation (2.19a). The resonance frequency Ω_1^{res} can subsequently be found from Equation (2.18). For very large mass ratios, Equation (2.19a) can be simplified to

$$\Omega_1^{\text{res}} = 2.065 e^{-0.3657H} \tag{2.19b}$$

which suggests that the resonance frequency decreases exponentially as H increases for $\mu \to \infty$. We further note that for a given H, the values of μ and β that result in resonance follow a simple linear relationship $\beta = a\mu + b$. Thus, for a given energy harvesting configuration featuring a cantilevered electroactive polymer strip and a passing vortex ring/pair, Equation (2.19) (in conjunction with the conversion strategy presented in §2.2, as required) can be used to inform the harvester selection to maximize the energy transferred to the structure. Herein, we have focused on cases where $\mu \geq 1$, which is generally valid for in-air energy harvesting. Though not shown, cases where $\mu < 1$ follow the same trend as in

Figure 9. However, due to the increased fluid-structural coupling effects as μ decreases, the computational time required for a converged solution increases.

Chapter 3

Energy harvesting from a vortex ring impinging on an annular ionic polymer metal composite [1]

In this chapter, we investigate the impact of a vortex ring with a thin, deformable, annular IPMC for energy harvesting. The vortex ring and the annulus are configured such that the center of the vortex ring is aligned with the hole in the annulus. An annulus is employed as opposed to a full IPMC disk to maximize the IPMC curvature during impact, which is proportional to the power output of the material. A similar configuration of a vortex ring interacting with a solid wall with a coaxially-aligned aperture in an ideal fluid is discussed in [104]. For an ideal fluid, vorticity is not generated along the solid wall or at the edge of

---

the aperture; the interaction of a vortex dipole with a semi-infinite plate [105] demonstrates the importance of induced vorticity on the interaction dynamics. Other studies involving vortex rings impacting walls in viscous fluids have also indicated the significant role of induced vorticity and the complex breakdown mechanics of the vortex ring [70, 106, 107].

The chapter is organized as follows: the problem and the modeling framework are introduced in detail in §3.1; and the experimental setup is illustrated in §3.2; results and discussion are presented in §3.3.

3.1 Problem Statement and Model Development

Herein, we explore the problem of a vortex ring propagating through a quiescent fluid and impacting an annular IPMC. A cylindrical coordinate system r, θ, and x is defined at the geometric center of the undeformed IPMC, with the longitudinal axis orthogonal to the plane of the annulus, see Figure 3.1. The vortex ring has initial core radius a_i, initial ring radius $R_\mathrm{r,i}$, and initial circulation Γ, and propagates through self-induction along the x axis in the negative x-direction as it approaches the annulus. The annulus has thickness h and is rigidly fixed at the outer radius R_o, while it is free at the inner radius R_i. The distance between the vortex ring and the annulus at any time t is given by $\xi(t)$, see Figure 3.1. As the vortex ring approaches the annulus, the ring radius and the core radius can vary in time. In an ideal fluid, the circulation is invariant, while in viscous flows the circulation is expected to continually decrease via viscous dissipation [84]. However, due to the short distance between the vortex ring creation and impact with the IPMC, we neglect variation in the circulation, which is always equal to Γ.

49
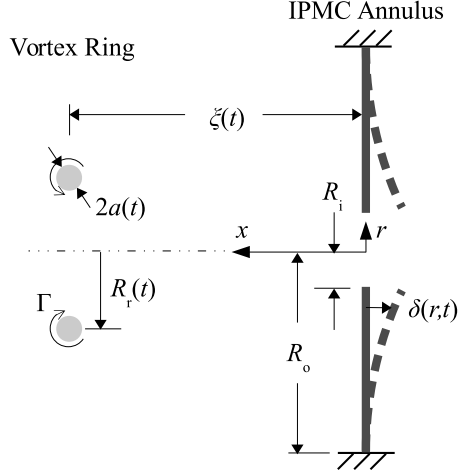
Figure 3.1: Schematic of the vortex ring and IPMC annulus configuration.

3.1.1 Structural Model

The thickness of the IPMC h is considerably smaller than the free vibration length $R_\mathrm{o} - R_\mathrm{i}$ and the deformation of the structure due to the vortex ring impact is assumed to be small, axisymmetric, and confined to the x direction. Thus, we model the IPMC as a Kirchhoff-Love plate undergoing axisymmetric bending [108]. The deflection of the plate is governed by

$$\rho h \ddot{\delta}(r,t) + D\left(\delta''''(r,t) + \frac{2}{r}\delta'''(r,t) - \frac{1}{r^2}\delta''(r,t) + \frac{1}{r^3}\delta'(r,t)\right) = -[\![p]\!](r,t) \qquad (3.1)$$

where $\delta(r,t)$ is the plate deflection in the x direction at time t, ρ is the IPMC mass density per unit volume, D is the bending stiffness, and $[\![p]\!](r,t)$ is the pressure difference across the plate produced by the vortex ring. Structural damping of the IPMC and viscous normal stresses of the fluid are neglected. In addition, the effect of electromechanical

50

coupling on the mechanical response of the IPMC is disregarded, as its contribution is negligible [16, 82]. The bending stiffness can be written in terms of the effective Young's modulus E and Poisson's ratio ν of the IPMC, namely, $D = Eh^3/(12(1 - \nu^2))$. The boundary conditions of the annulus are

$$\delta(R_\mathrm{o}, t) = 0 \tag{3.2}$$

$$\delta'(R_\mathrm{o}, t) = 0$$

$$\delta''(R_\mathrm{i}, t) + \frac{\nu}{R_\mathrm{i}} \delta'(R_\mathrm{i}, t) = 0$$

$$\delta'''(R_\mathrm{i}, t) - \frac{1}{R_\mathrm{i}^2} \delta'(R_\mathrm{i}, t) + \frac{1}{R_\mathrm{i}} \delta''(R_\mathrm{i}, t) = 0$$

and the plate is initially at rest, $\delta(r, 0) = 0$, when the vortex ring is generated.

Employing the initial vortex ring radius $R_\mathrm{r,i}$ as a length scale, $\Gamma/R_\mathrm{r,i}$ as a velocity scale, $R_\mathrm{r,i}^2/\Gamma$ as a time scale, and $\varrho\Gamma^2/R_\mathrm{r,i}^2$, where ϱ is the fluid density, as a pressure scale, Eq. 3.1 can be written as

$$\ddot{\tilde{\delta}}(\tilde{r}, \tilde{t}) + K\left(\tilde{\delta}''''(\tilde{r}, \tilde{t}) + \frac{2}{\tilde{r}}\tilde{\delta}'''(\tilde{r}, \tilde{t}) - \frac{1}{\tilde{r}^2}\tilde{\delta}''(\tilde{r}, \tilde{t}) + \frac{1}{\tilde{r}^3}\tilde{\delta}'(\tilde{r}, \tilde{t})\right) = -\mu^{-1}[\![\tilde{p}]\!](\tilde{r}, \tilde{t}) \tag{3.3}$$

Here, $\mu = \rho h/(\varrho R_{r,i})$ is the mass ratio, $K = D/(\rho h \Gamma^2)$ is the dimensionless bending stiffness, and the tilde indicates nondimensional variables. The boundary conditions for the plate in dimensionless form are

$$\tilde{\delta}(R_\mathrm{o}/R_\mathrm{r,i}, \tilde{t}) = \tilde{\delta}'(R_\mathrm{o}/R_\mathrm{r,i}, \tilde{t}) = \tilde{\delta}''(R_\mathrm{i}/R_\mathrm{r,i}, \tilde{t}) + \frac{\nu}{R_\mathrm{i}/R_\mathrm{r,i}}\tilde{\delta}'(R_\mathrm{i}/R_\mathrm{r,i}, \tilde{t})$$

$$= \tilde{\delta}'''(R_\mathrm{i}/R_\mathrm{r,i}, \tilde{t}) - \frac{1}{R_\mathrm{i}/R_\mathrm{r,i}^2}\tilde{\delta}'(R_\mathrm{i}/R_\mathrm{r,i}, \tilde{t}) + \frac{1}{R_\mathrm{i}/R_\mathrm{r,i}}\tilde{\delta}''(R_\mathrm{i}/R_\mathrm{r,i}, \tilde{t}) = 0 \tag{3.4}$$

and the initial condition reads as $\tilde{\delta}(\tilde{r}, 0) = 0$. For the remainder of the document the tilde notation is omitted for convenience and all variables are presented in dimensionless form unless otherwise stated.

3.1.2 Fluid Model

The fluid encompassing the IPMC is modeled as inviscid, incompressible, and irrotational except in the core of the vortex ring. Assuming that the outer radius of the annulus R_o is large compared with the ring dimensions, the annulus can be approximated as an infinite wall with an aperture. Further, assuming that the IPMC deflection is sufficiently small to have negligible influence on the flow field, the potential function governing the fluid flow for $x \geq 0$, following [104], can be written in nondimensional form as

$$\phi_+(x, r, t) = \phi_\mathrm{vr}(x, r, t) + \phi_\mathrm{img}(x, r, t) + \phi_\mathrm{ap}(x, r, t) \tag{3.5}$$

where

$$\phi_\mathrm{vr}(x, r, t) = -\frac{R_\mathrm{r}(t)}{2R_\mathrm{r,i}} \int_0^\infty \mathrm{e}^{-k(\xi(t)/R_\mathrm{r,i} - x)} J_0(kr) J_1\left(k\frac{R_\mathrm{r}(t)}{R_\mathrm{r,i}}\right) \mathrm{d}k \tag{3.6}$$

is the potential function for the vortex ring,

$$\phi_\mathrm{img}(x, r, t) = -\frac{R_\mathrm{r}(t)}{2R_\mathrm{r,i}} \int_0^\infty \mathrm{e}^{-k(\xi(t)/R_\mathrm{r,i} + x)} J_0(kr) J_1\left(k\frac{R_\mathrm{r}(t)}{R_\mathrm{r,i}}\right) \mathrm{d}k \tag{3.7}$$

is the image ring used to create the wall, and

$$\phi_{\text{ap}}(x, r, t) = \frac{\beta R_{\text{r}}(t)}{\pi R_{\text{r,i}}} \int_0^\infty \int_0^\infty \int_0^1 e^{-k\xi(t)/R_{\text{r,i}} - \lambda x} J_0(\lambda r) J_1\left(k\frac{R_{\text{r}}(t)}{R_{\text{r,i}}}\right)$$
$$\times \cos(\beta k s) \cos(\beta \lambda s) \mathrm{d}s \mathrm{d}\lambda \mathrm{d}k \qquad (3.8)$$

is a correction for the aperture. Here, ξ is the distance of the ring from the annulus, as defined in Figure 3.1, J_α is the Bessel function of the first kind of order α and $\beta = R_{\text{i}}/R_{\text{r,i}}$ relates the hole size to the initial ring radius. We assume zero net flux through the aperture in the absence of the vortex ring, which eliminates a term in the potential function presented in [104]. The potential function in the $x < 0$ half-space is given by

$$\phi_-(x, r, t) = -\frac{\beta R_{\text{r}}(t)}{\pi R_{\text{r,i}}} \int_0^\infty \int_0^\infty \int_0^1 e^{-k\xi(t)/R_{\text{r,i}} + \lambda x} J_0(\lambda r) J_1\left(k\frac{R_{\text{r}}(t)}{R_{\text{r,i}}}\right)$$
$$\times \cos(\beta k s) \cos(\beta \lambda s) \mathrm{d}s \mathrm{d}\lambda \mathrm{d}k \qquad (3.9)$$

These potential functions satisfy the boundary conditions of equal pressures and x velocities at the aperture $(r/\beta < 1)$ and null x velocity along the plate $(r/\beta > 1)$.

The velocity field at any point in the domain can be obtained from

$$u = \frac{\partial \phi}{\partial x}; \qquad v = \frac{\partial \phi}{\partial r} \qquad (3.10)$$

where u and v are the nondimensional longitudinal and radial velocity components, respectively. Note that for $x \geq 0$ the velocities are found from the potential function ϕ_+, while the gradient of ϕ_- provides the velocities for $x < 0$. The nondimensional pressure

53

difference across the annulus can be computed from the unsteady Bernoulli equation as [85]

$$\llbracket p_0 \rrbracket(r,t) = -\frac{U_+^2(r,t)}{2} - \dot{\phi}_+(r,t) + \frac{U_-^2(r,t)}{2} + \dot{\phi}_-(r,t) \tag{3.11}$$

where $U^2 = u^2 + v^2$.

Equation 3.11 rests upon the assumption that the IPMC is blocked during the impact and thus neglect added mass and damping effects associated with the IPMC vibration [109]. To indirectly account for the IPMC motion and more closely interpret experimental findings, we propose to modify Eq. 3.11 by including on the right hand side an added mass effect $H(r,t)$ proportional to the acceleration of the IPMC. Specifically, we assume that the pressure jump across the IPMC is

$$\llbracket p \rrbracket(r,t) = \llbracket p_0 \rrbracket(r,t) + H(r,t) \tag{3.12}$$

where $\llbracket p_0 \rrbracket$ is given in Eq. 3.11 and the added mass contribution is described in §3.1.5 when analyzing the IPMC vibration based upon [110].

3.1.3 Electrical Model

The IPMC electromechanical behavior is described using a black box model [111–113] consisting of the series connection of a voltage source that depends on the mean curvature of the IPMC, a resistor R_{IPMC}, and a capacitor C_{IPMC}. Specifically, the voltage source is $V_{\text{d}}(t) = \gamma\kappa(t)$, where γ is a sensing gain which is determined from experimental data and $\kappa(t) = \frac{2}{R_{\text{o}}^2 - R_{\text{i}}^2}(R_{\text{o}}\delta'(R_{\text{o}},t) - R_{\text{i}}\delta'(R_{\text{i}},t))$ is the mean IPMC curvature [108]. The IPMC

resistance and capacitance are related to the counterion diffusion in the IPMC core and double layer phenomena taking place at the electrodes. Both these parameters are identified from experiments on IPMC step response following [82]. In our study, we focus on the case of short-circuited electrodes.

Based on the proposed lumped circuit model and assuming that the IPMC is initially discharged, the short-circuit current $I_{\mathrm{sc}}(t)$ is given by

$$I_{\mathrm{sc}}(t) = \frac{\gamma\kappa(t)}{R_{\mathrm{IPMC}}} - \frac{\int_0^t \gamma\kappa(t-\tau)e^{-\frac{\tau}{C_{\mathrm{IPMC}}R_{\mathrm{IPMC}}}}\,\mathrm{d}\tau}{C_{\mathrm{IPMC}}R_{\mathrm{IPMC}}^2} \tag{3.13}$$

Estimates of power harvesting when the IPMC electrodes are shunted with a resistor can be obtained following [17].

3.1.4 Energy Transfer

Assuming the vortex core to be thin in comparison with the radius, its energy can be estimated by following [43] as

$$E_{\mathrm{vr}}(t) = \frac{1}{2}\varrho\Gamma^2 R_{\mathrm{r}}(t)\ln\left(\frac{8R_{\mathrm{r}}(t)}{a(t)} - 2.05\right) \tag{3.14}$$

To elucidate the possibility of energy harvesting, we compare the energy of the vortex core with the energy dissipated in the IPMC resistance during the impact, which is estimated from the short-circuit current as

$$E_{\mathrm{IPMC}} = R_{\mathrm{IPMC}}\int_0^\infty I_{\mathrm{sc}}^2(t)\mathrm{d}t \tag{3.15}$$

55

3.1.5   Solution Procedure

The problem is solved by assuming uni-directional coupling between the fluid and the IPMC, whereby the vortex dynamics results in a structural deformation, which does not perturb the fluid flow. Thus, the fluid flow is solved independently through the procedure described in §3.1.2 to obtain the contribution to the pressure loading on the annulus associated with the vortex ring approaching the annulus. The IPMC deformation is computed using modal analysis. Specifically, the fluid loading is projected onto the free vibration mode shapes of the annulus, and the amplitude of each mode shape is independently computed. Thus, we write the plate deflection as

$$\delta(r,t) = \sum_{n=1}^{\infty} a_n(t)\Delta_n(r) \tag{3.16}$$

where $\Delta_n(r)$ is the nth mode shape of the annulus with eigenvalue λ_n and $a_n(t)$ is its corresponding amplitude. Expressions for the mode shapes and eigenvalues can be found in [108]. The expansion in Eq. 3.16 is substituted into Eq. 3.3, which is, in turn, projected on the annulus mode shapes by multiplying both sides of the equation by $\Delta_m(r)$ and integrating from $R_{\text{i}}/R_{\text{r,i}}$ to $R_{\text{o}}/R_{\text{r,i}}$, with $m = 1, 2, \ldots$. By considering the orthogonality of the mode shapes we have

$$\ddot{a}_m(t) + K\left(\frac{\lambda_m R_{\text{r,i}}}{R_{\text{o}}}\right)^4 a_m(t) = -\mu^{-1}\int_{R_{\text{i}}/R_{\text{r,i}}}^{R_{\text{o}}/R_{\text{r,i}}} (\llbracket p_0 \rrbracket(r,t) + H(r,t))\,\Delta_m(r) r\mathrm{d}r \tag{3.17}$$

Ultimately, the IPMC deflection is replaced in Eq. 3.13 to calculate the short-circuit current. Based on the time scale of the process, only two modes are retained in the

56

expansion. The modal contributions of the added mass, found by [110] for an annulus oscillating along its axis of symmetry in an ideal fluid, are $-\mu^{-1}\int_{R_i/R_{r,i}}^{R_o/R_{r,i}} H(r,t)\Delta_1(r)r\mathrm{d}r = -\mu^{-1}(R_o/R_{r,i})\ddot{a}_1(t)$ and $-\mu^{-1}\int_{R_i/R_{r,i}}^{R_o/R_{r,i}} H(r,t)\Delta_2(r)r\mathrm{d}r = -(1/2)\mu^{-1}(R_o/R_{r,i})\ddot{a}_2(t)$.

3.2 Experimental Scheme

Experiments are conducted in a custom vortex ring facility consisting of a piston/cylinder vortex generator in a quiescent tank, see Figure 3.2a. The acrylic tank is $91 \times 61 \times 61\,\mathrm{cm}^3$ and the outlet of the sharp-edged vortex generator is located approximately $30\,\mathrm{cm}$ from the edge of the tank. The main piston/cylinder has inner diameter of $10.2\,\mathrm{cm}$, though the outlet at the location of the vortex ring formation has a diameter of $12.7\,\mathrm{mm}$. The piston is actuated by a DC motor (Boston Gear PM9100ATF-1) attached to a motor controller (Electro-Craft DC-35L) and controlled with a custom open loop LabVIEW VI. The motor is electrically and mechanically isolated from the rest of the facility to minimize electrical coupling and vibrations.

Vortex rings of various strength are formed by controlling the piston stroke length [40]. The IPMC annulus is clamped in a custom fixture rapid-prototyped in ABS plastic. Aluminum electrodes are flush-mounted on each side of the clamp to provide electrical connectivity. The two sides of the clamp are held together firmly with the IPMC between them using nylon bolts, see Figure 3.2b. The outer annulus radius is fixed by the clamp geometry at $R_o = 28.6\,\mathrm{mm}$. The IPMC clamp is rigidly fixed to the acrylic tank via an aluminum scaffolding built over the top of the tank. We note that while inserting the IPMC into the clamp it is difficult to maintain uniform tension on the IPMC to keep it
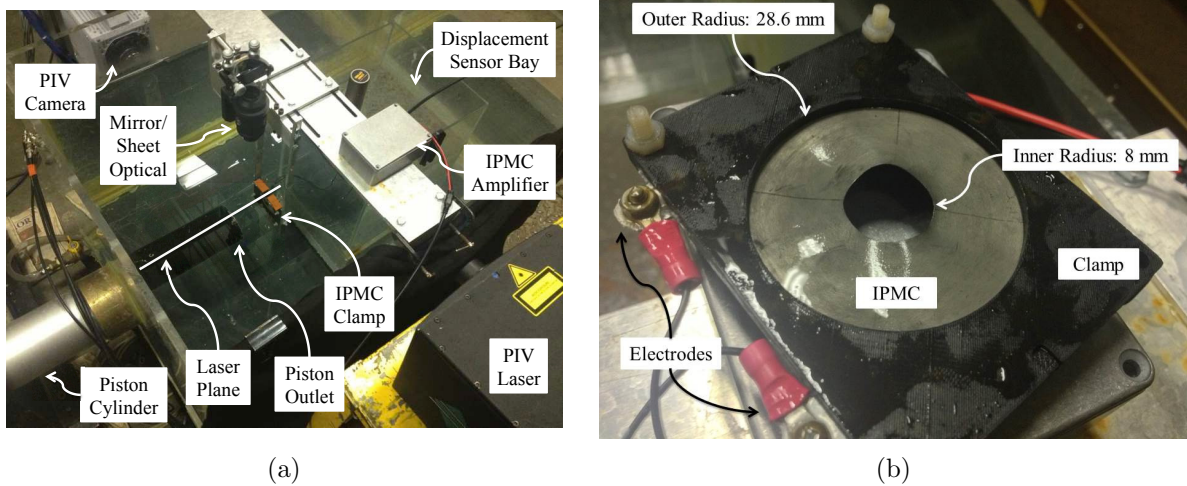
Figure 3.2: (a) Image of the experimental setup, and (b) close-up of the IPMC in the clamp.

perfectly flat, particularly since IPMCs are susceptible to tearing. As such, minor warping of the IPMC after installation into the clamp occurs, as seen in Figure 3.2b.

The vortex ring characteristics, including translation speed, approximate core radius, and circulation are measured using a LaVision Inc. time-resolved particle image velocimetry (PIV) system, for the operational theory of PIV see for example [114, 115]. The PIV system consists of a Photron Fastcam SA-4 CMOS camera with a 1k by 1k pixel array and a maximum frame rate of 3600 frames per second at full resolution. The flow is illuminated with a 20 mJ/pulse Photonics Industries DM20-527 single cavity diode pumped Nd:YLF laser with a 1 kHz repetition rate. The laser is spread into a sheet using an array of negative and positive cylindrical and spherical lenses and is aligned with the center of the vortex ring, see Figure 3.2a. A mirror is used to enable illumination of the fluid upstream and downstream of the IPMC annulus, and the camera is arranged orthogonal to the laser

sheet. We note that the clamp is not optically clear, and thus data are not recorded in this region.

An in-house manufactured Nafion-core platinum-electrodes IPMC is used in these experiments. The overall IPMC dimensions are $66 \times 68 \times 0.2 \, \mathrm{mm}^3$. A hole of radius $R_\mathrm{i} = 8.0 \, \mathrm{mm}$ is cut out of the center of the IPMC which, when placed concentrically into the clamp, serves as the inner edge of the annulus. The IPMC density and Young's modulus are assumed to be $2126 \, \mathrm{kg/m}^3$ and $497 \, \mathrm{MPa}$ from [15]. The Poisson ratio is estimated from [116] to be $\nu = 0.487$. The IPMC capacitance and resistance are directly measured following the procedure in [82] and are equal to $C_\mathrm{IPMC} = 1.005 \, \mathrm{mF}$ and $R_\mathrm{IPMC} = 96.8 \, \Omega$, respectively. During vortex impact, the circuit presented in Figure 3.3 is employed to measure the short-circuit current. The circuit consists of two $9 \, \mathrm{V}$ batteries as the power supply, a UA741CN operational amplifier and a $1 \, \mathrm{k}\Omega$ resistor in an inverting current voltage amplification configuration. The amplification circuit has a nominal gain of $1000 \, \mathrm{V/A}$, whereby a minute input of $1 \, \mu\mathrm{A}$ of short-circuit current is scaled to a measurable voltage output of $1 \, \mathrm{mV}$. The batteries are used in lieu of a traditional power supply to improve the signal-to-noise ratio by providing ground isolation to the IPMC and amplification circuit.

The displacement of the annulus due to the impact is measured using a laser Doppler vibrometer (Wenglor OCP162H0180). The vibrometer laser is focused at a point $2 \, \mathrm{mm}$ from the inner edge of the annulus. To avoid interference between the vibrometer and PIV, optical filters are used for removing the influence of one from the other. The vibrometer is calibrated for use in water using a target affixed to a translation stage. A series of band stop and low pass filters are used to condition the displacement signal.

In this study, vortex rings of two different strengths are propelled towards the IPMC
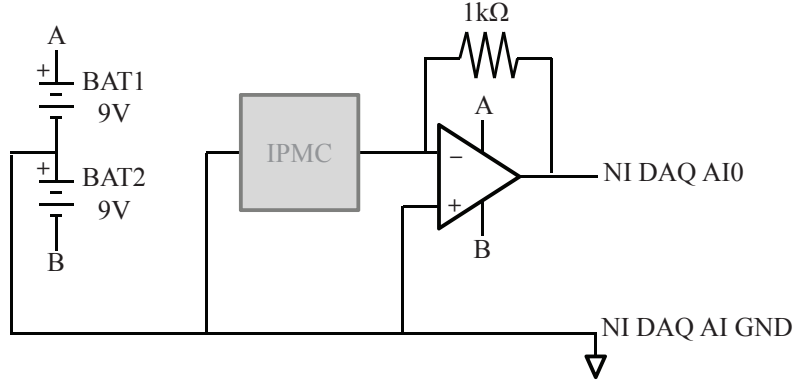
Figure 3.3: Amplification circuit used for the energy harvesting experiments.

annulus. Each vortex ring has an initial radius of $R_{r,i} = 11.4\,\text{mm}$, which is dictated by the dimensions of the piston/cylinder exit. The vortex ring circulation is computed from

$$\Gamma = \oint_C \mathbf{u} \cdot d\mathbf{l} \tag{3.18}$$

where $\mathbf{u}$ is the fluid velocity vector, whose components are u and v, and $d\mathbf{l}$ is a differential line element along the contour C. The circulation data are extracted from the PIV results by evaluating Eq. 3.18 along a square contour surrounding the core of the vortex ring in the two-dimensional plane through the vortex ring center. Tests at both vortex ring circulations are repeated 5 times, with the nominal circulations with standard deviation for the cases being 3039 ± 100 and $5069 \pm 333\,\text{mm}^2/\text{s}$, respectively, at a distance of $\approx 20\,\text{mm}$ from the IPMC. The standard deviation in these experiments is in part due to the uncertainty in estimating the circulation from the PIV data.

A third lower circulation was also tested, but was insufficient to measurably deflect the annulus and is thus not included in this paper. Furthermore, other larger annulus geometry

ratios ($R_\mathrm{i}/R_\mathrm{o}$) were also studied, however these also failed to result in any deflection due to the reduced vibration length. As such, only the smallest annulus geometry ($R_\mathrm{i}/R_\mathrm{o} = 0.28$) at the two circulation levels are presented herein.

3.3   Experimental Results

The vortex ring velocity and vorticity fields are presented in Figure 3.4 for a representative experiment for both of the vortex ring circulation strengths. The top row (Figure 3.4a–3.4c) shows the lower strength ring at three locations, while the bottom row (Figure 3.4d–3.4f) displays the higher strength ring at similar locations. Note that since the advection speed of the higher strength ring is larger than that of the lower strength ring, the physical time between frames for the top and bottom rows are not the same. The gray block in each frame of the figure indicates the position of the clamp holding the IPMC, which is not optically clear. Consequently, the velocity field within this region is not measured. The same vorticity scale is applied to all frames for comparison.

The vortex ring core is clearly evident in the vorticity contours, appearing as counter-rotating vortices in the PIV slice. The associated velocity field is shown in the overlaid vectors. The vortex ring propagates towards the IPMC due to self-induction. The regions of concentrated vorticity are larger for higher circulation case, as seen by comparing images in the same column in Figure 3.4; that is, Figure 3.4a versus Figure 3.4d. Trailing vorticity is observed behind the vortex ring for both circulation levels in Figure 3.4b and 3.4e, with the wake being more pronounced for the stronger ring. This trailing wake occurs when the stroke-to-diameter ratio of the piston, referred to as the formation number, is greater than
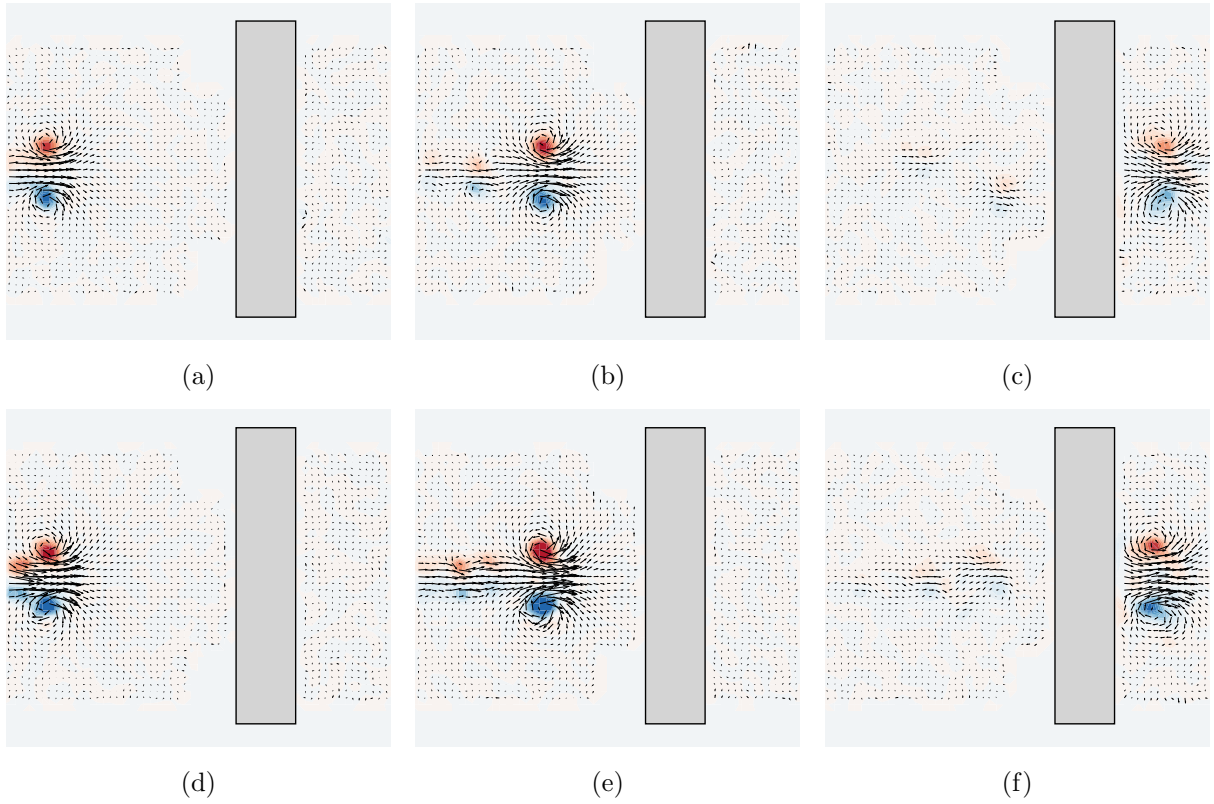
Figure 3.4: Velocity and vorticity fields showing the vortex ring pre- and post-impact for the $\Gamma = 3039, \mathrm{mm^2/s}$ (top row) and $\Gamma = 5069\,\mathrm{mm^2/s}$ (bottom row) vortex rings. The maximum and minimum vorticity contours correspond to $\pm 100\,\mathrm{s^{-1}}$, respectively. The gray block indicates the location of the IPMC clamp, which is not optically clear.

approximately 4 [40]. In this case, the vortex ring is unable to entrain all of the vorticity shed from the end of the cylinder during the formation process and consequently pinches off prior to the piston reaching the end of its stroke. The remaining vorticity then forms into a trailing wake as a series of smaller, connected rings, see [40].

The final column of Figure 3.4 suggests that the vortex ring survives the interaction with the IPMC annulus. This, however, is very unlikely, since vorticity induced along the

annulus will interact once the ring is close, which will, in turn, lead to break down of the original ring [15]. Perhaps, the velocity field induced by the primary ring causes fluid to pass through the hole, which results in vorticity production at the edge of the hole. This vorticity subsequently rolls up into the secondary vortex ring observed in Figure 3.4c and 3.4f. The circulation of the secondary vortex ring is $2067 \pm 152\,\mathrm{mm}^2/\mathrm{s}$ for the lower initial circulation and $3312 \pm 238\,\mathrm{mm}^2/\mathrm{s}$ for the higher initial case. In both cases, this secondary ring has circulation approximately 33% lower than that of the initial primary ring, with individual experiments ranging from $26 - 40\%$.

The displacement of the IPMC annulus 2 mm from the free edge and the measured short-circuit current during impact are presented in Figure 3.5 for all conducted experiments. In all cases, the IPMC initially displaces towards the approaching vortex ring, indicated by the initial positive displacement. Were the IPMC a full disk as opposed to an annulus, the stagnation pressure at the center of the disk due to the induced fluid motion would likely push the plate away from the oncoming vortex ring, as observed in two-dimensional potential flow of a vortex pair approaching the center of a deformable plate [72]. However, since the vortex ring is aligned with the center of the annulus and the ring radius is on the order of the hole size, it is the lower pressure region associated with the vortex ring core that initially interacts with the annulus, causing the IPMC to pull towards the approaching ring. This is similar to the findings in [76], in which a horizontally oriented cantilevered beam is drawn towards the low pressure core of a vortex ring as it passes over the beam. Upon impact, however, the annulus is strongly pushed away from the ring as some of its momentum is transferred to the structure. This is particularly evident for the stronger ring in Figure 3.5b, which has a large negative deflection. After impact, the motion of the

structure is rapidly damped by the surrounding fluid and the annulus returns to rest.
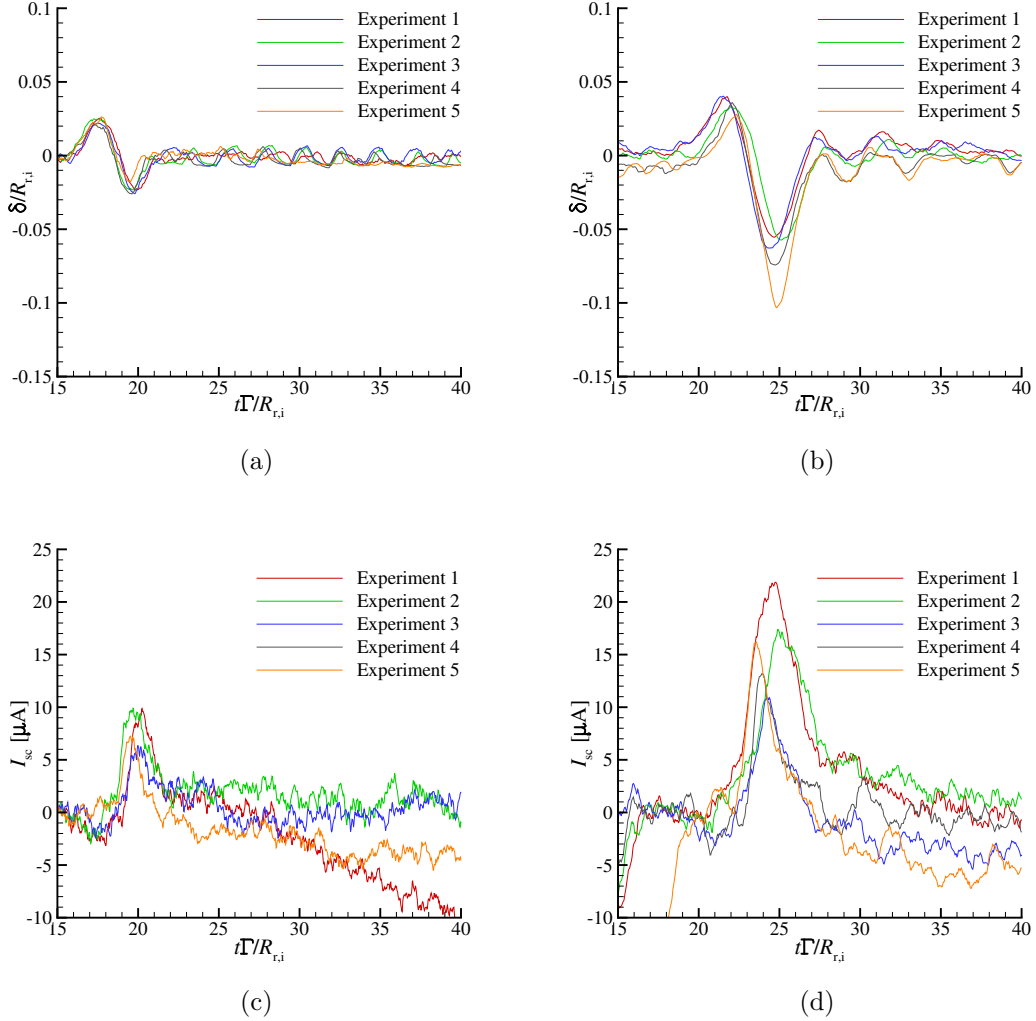

Figure 3.5: IPMC normalized deflection at the initial ring radius (top row) and short-circuit current (bottom row) for the low (left column) and high (right column) circulation experiments. All five experiments are shown in each plot.

The short-circuit current (Figure 3.5c and 3.5d) roughly follows the magnitude of the

displacement curves. As the IPMC starts to mechanically deform due to the interaction with the vortex ring, the current measured through the IPMC begins to increase. The peak in the measured current correlates with the peak in the displacement magnitude. The current decays quickly, as the mechanical deformation reduces after the impact. The results of all experiments, including pre- and post-impact vortex ring circulation, maximum deflection, and maximum current are tabulated in Table 3.1.

$\Gamma_{\mathrm{pre}}\,[\mathrm{mm}^2/\mathrm{s}]$	$\Gamma_{\mathrm{post}}\,[\mathrm{mm}^2/\mathrm{s}]$	$\frac{\Gamma_{\mathrm{pre}}-\Gamma_{\mathrm{post}}}{\Gamma_{\mathrm{pre}}}\,[\%]$	$\delta_{\max}\,[\mathrm{mm}]$	$I_{\max}\,[\mu\mathrm{A}]$
Low Circulation				
2945	1835	37.7	0.23	9.87
3205	1994	37.8	0.26	9.89
2983	2157	27.7	0.28	6.35
3022	2208	26.9	0.28	6.58
3040	2142	29.5	0.18	7.24
High Circulation				
4875	2986	38.7	0.65	21.9
4719	3258	31.0	0.66	17.4
4900	3624	26.0	0.75	10.9
5413	3252	39.9	0.75	13.2
5437	3441	36.7	1.13	16.2

Table 3.1: Summary of key experimental results. Here, Γ_{pre} is the pre-impact vortex ring circulation computed when the ring is $\approx 20\,\mathrm{mm}$ upstream of the IPMC, Γ_{post} is post-impact vortex ring circulation computed when the ring $\approx 10\,\mathrm{mm}$ downstream of the IPMC, $\delta_{\max}$ is peak displacement magnitude, and $I_{\max}$ is peak measured current.

Using the experimentally derived vortex ring circulation, radius, and core radius, the trajectory and deformation of the ring as it approaches an annulus in an ideal fluid can be computed using the model described in §3.1.2. The vortex ring position, ring radius, and

core radius are presented in Figure 3.6 for both the high and low circulation cases. For both considered ring strengths, as the ring approaches the annulus its radius starts to increase. In order to conserve circulation of the vortex core, the core radius decreases accordingly, see Figure 3.6b. Once the ring gets very close to the annulus, its motion is dominated by the image vortex ring and its radius begins to increase rapidly. Note that in the absence of viscosity, the ring radius continues to increase without bound while the distance of the ring from the annulus asymptotically approaches a fixed value (Figure 3.6a); this is analogous to the canonical problem of a pair of point vortices approaching a wall and subsequently splitting apart and moving away from one another, see for example [84]. The initial rate of approach is faster for the higher circulation ring, as expected, and upon reaching the plate its radius grows faster than the lower circulation case. We note that while for these test cases the vortex ring grows as it approaches the plate, for larger hole-to-ring diameter ratios the vortex ring may instead pass through the hole [104]. In addition, the secondary vortex ring observed experimental (Figure 3.4(c) and (f)) is not captured in this inviscid model.

The predicted annulus deflection from the theoretical model is compared with experimental results in Figure 3.7a and 3.7b for both the high and low circulation cases. Experiment 2 from Figure 3.5 for both circulation levels is selected as a representative case for comparison with model predictions. Predictions for the IPMC deflection at the inner radius fail to capture the initial "pulling" on the annulus by the vortex ring observed in the experiment. This is likely due to the fact that the model is based on an ideal fluid solution as well as the fact that it does not include structural deformations in the computation of the fluid flow. Nevertheless, the agreement between the model and the experiments for the
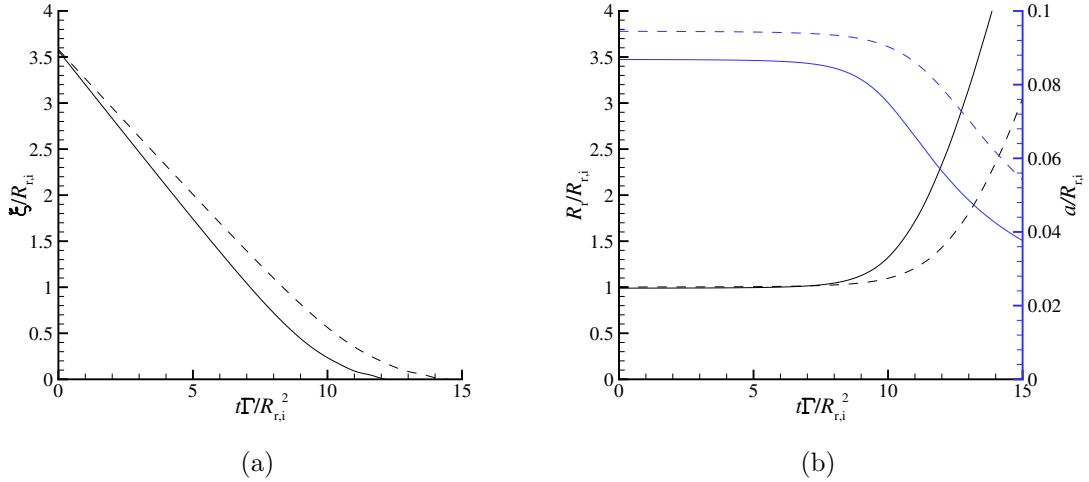
66

Figure 3.6: (a) Trajectory and (b) ring and core radius for the high (solid line) and low (dashed line) cases. In (b), the top two lines correspond to the right ordinate, while the bottom two lines correspond to the left ordinate.

peak deflection after the impact is satisfactory, for both the low and high circulation cases. While the peak values from the model overestimate the experimental values by $50-100\%$ in some cases, we deem this to be good agreement based upon the difficulty achieving repeatable results experimentally, as well as the uncertainty in material properties used in the modeling. Since structural and fluid damping are not included in the model, once the plate is set in motion by the impact it continues to vibrate differently from experimental observations.

Figure 3.7c and 3.7d display the predicted short-circuit current corresponding to the low and high circulations cases shown in Figure 3.7a and 3.7b with coupling coefficient $\gamma = -0.00162\,\mathrm{V\,m}$. The latter coefficient is computed by averaging identified coupling coefficients from all of the 10 experiments in Figure 3.5. The coefficient of determination
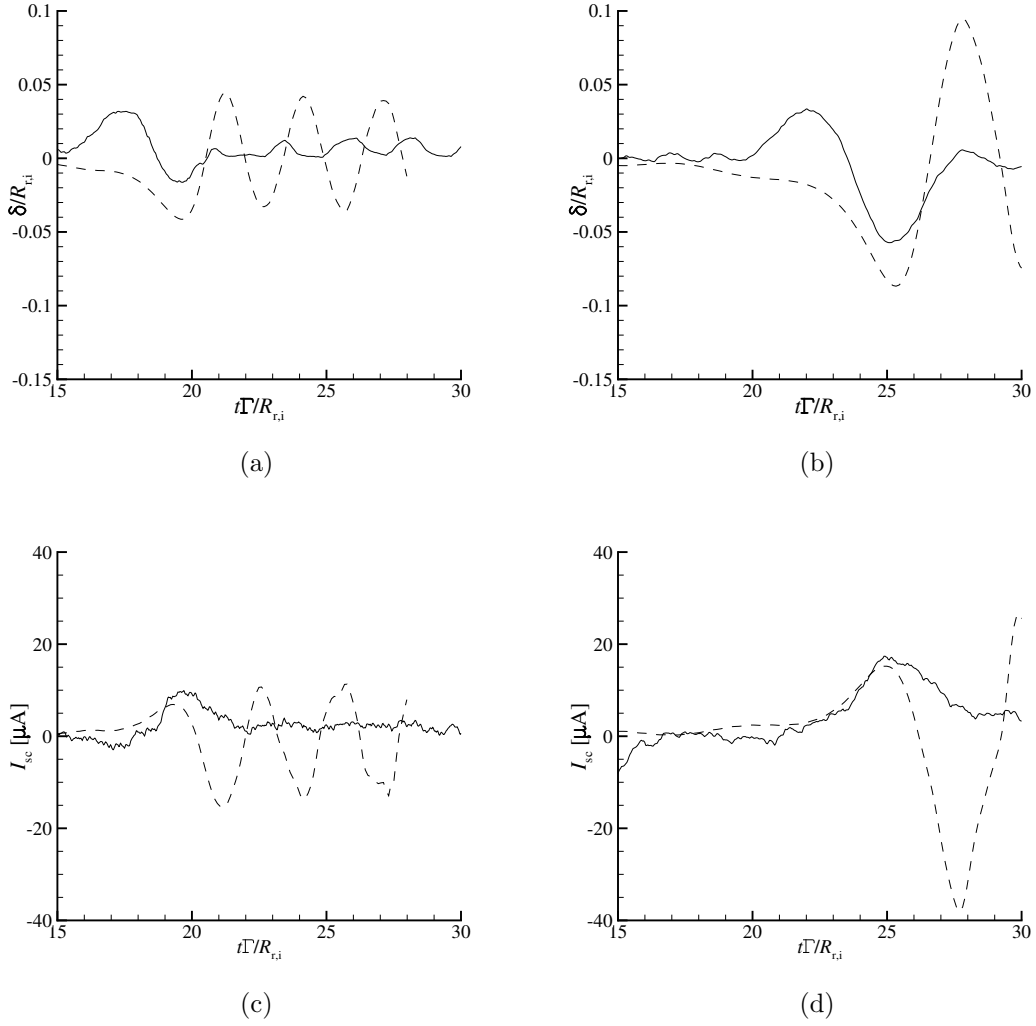
Figure 3.7: Comparison of model predictions (dashed lines) with experimental data (solid lines) for normalized plate deflection at the initial ring radius (top row) and short-circuit current (bottom row) for the low (left column) and high (right column) circulation experiments.

of the data fit to the experiments is $R^2 = 0.64$, indicating some variation between the experiments. We note that the predicted short-circuit current is in good agreement with the

experimentally measured values for both the low and high circulation cases. As evidenced from the experiments, the peak current coincides with the peak deflection. The model then predicts an alternating current as the plate vibrates back and forth in the absence of damping.
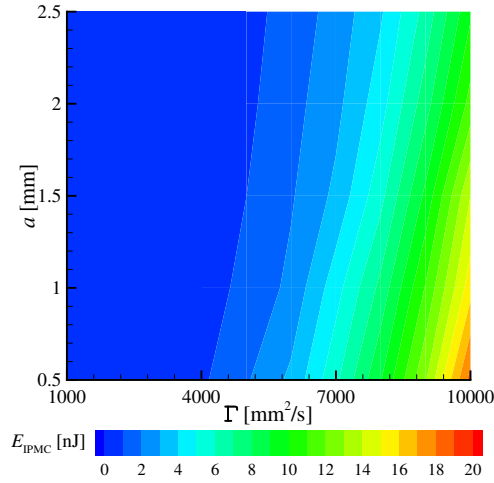

Figure 3.8: IPMC energy versus vortex ring circulation and core radius from the analytical model.

The energy of the IPMC as a function of vortex ring circulation and core radius for a fixed ring radius of $R_{r,i}$ is presented in Figure 3.8 using dimensional values. As the vortex ring circulation increases, the energy transferred to the IPMC increases. This increase is slightly more rapid for smaller vortex ring core radii, though the dependence overall on core radius is small. The energy transfer to the IPMC from the vortex ring in the experiments is presented in Table 3.2. Comparison of these experimental data with Figure 3.8 indicates that the model is successful in anticipating the effect of circulation on energy transfer to the IPMC. To estimate the efficiency of such energy transfer, we calculate the ratio between

69

the vortex ring energy computed from Eq. 3.14 and the experimental values of the energy transfer to the IPMC in Table 3.2. In all experiments, approximately 0.0001-0.001% of the ring energy is transduced into electrical energy that is dissipated in the IPMC. We note that such conversion ratio is comparable with similar studies involving vortex rings impacting IPMCs [72]. The relatively low energy transduction rates are expected to improve with continued advancement of IPMC manufacturing techniques and further understanding of its sensing modality. As of now, the limited energy conversion may be more valuable in the design of underwater sensors rather than energy scavenging devices. While the analysis presented herein is focused on harvesting using IPMCs, the proposed methodology, which includes modeling the vortex ring and its interaction with the annulus, as well as the electrical transduction, is expected to find application in the design of energy scavenging devices incorporating other soft electroactive materials, such as polyvinylidene fluoride (PVDF). For a comparison between IPMCs and PVDF, see [117].

$\Gamma \, [\mathrm{mm}^2/\mathrm{s}]$	$E_{\mathrm{vr}} \, [\mu\mathrm{J}]$	$E_{\mathrm{IPMC}} \, [\mathrm{nJ}]$	Transfer Ratio [%]
Low Circulation			
2945	98	0.41	0.00041
3205	149	0.47	0.00031
2983	92	0.22	0.00023
3022	126	0.12	0.00009
3040	144	0.15	0.00010
High Circulation			
4875	365	2.80	0.00076
4719	319	1.59	0.00049
4900	329	0.39	0.00011
5413	381	0.51	0.00013
5437	357	2.58	0.00072

Table 3.2: Energy harvested from the impinging vortex ring by the IPMC. Vortex ring circulation and energy is computed when the ring is $\approx 20\,\mathrm{mm}$ from the IPMC.

Chapter 4

Conclusions

Energy harvesting from a passing vortex ring using a cantilevered smart material plate, and from an impacting vortex ring using an annular disk were examined. For the former, a coupled, inviscid, two-dimensional fluid-structure interaction model was developed for the cantilevered plate configuration, in which the plate was oriented parallel to and offset from the path of the vortex ring in an otherwise quiescent fluid. The model was validated against the experimental result, and employed to optimize the fluid to structure energy transfer. In the latter study, the concentric impact of a vortex ring to an IPMC annular disk was experimentally investigated and compared with a simplified model. The findings of each configuration were summarized in the following sections.

4.1 Energy harvesting from a passing vortex ring using a cantilevered smart material plate

The energy harvesting configuration of a vortex ring passing a cantilevered plate was studied using the coupled two-dimensional fluid-structure analytical solution developed by Peterson and Porfiri [73], which modeled the fluid domain with the potential flow theory and the structure with the Kirchhoff-Love plate theory. In pursuance of analyzing the three-dimensional problem with the two-dimensional model, a method of converting the three-dimensional vortex ring/plate configuration into a two-dimensional vortex pair/plate representation was developed. The analytical result was compared with a recent experimental study conducted by Goushcha *et al.* [76]. The model predictions of the plate kinematics and the fluid induced pressure loading on the plate were consistent with the experimental measurements.

The analytical model was applied to a parametric study aimed at optimizing the energy transferred from a given vortex ring to the plate. The key optimization parameter of dimensionless plate natural frequency was established using the classical analysis of a point load moving along a plate, which indicated that the resonance frequency occurs at a specific ratio between the plate natural frequency and the convective time scale of the moving load. The parametric study presented the fluid to structure energy transfer for a given mass ratio as a function of the dimensionless plate frequency. The parametric study demonstrated a significant increase in energy transfer at the resonance frequency, as well as the decrease of resonance frequency towards asymptote as the mass ratio increases. Additionally, a second parametric study examined the change in the resonant frequency

with respect to the change in the distance between the vortex pair and the plate. It was concluded that the resonant frequency shifts towards lower values as the distance increases.

From the result of the parametric studies, an empirical correlation for the shift in resonant frequency with reference to mass ratio, dimensionless bending stiffness and distance from the vortex pair to the plate was formulated. The correlation, along with the three-dimension to two-dimension conversion scheme, can be used to determine the plate properties for a given passing vortex condition to achieve optimal energy transfer. The result of the parametric studies also underlined the critical importance of the convective time scale of the passing vortices in relation to the plate natural frequency for this type of vortex-deformable structure interactions.

4.2 Energy harvesting from an impacting vortex ring using an annular smart material disk

The energy harvesting configuration of a vortex ring impacting a concentric deformable IPMC annulus was examined experimentally. The initial pulling of the annular disk as the vortex ring approaches was observed from the experimental findings, likely caused by the low pressure of the vortex core. Further, upon impact of the vortex ring, the plate was pushed by the vortex ring, then, a secondary vortex ring was detected. The secondary vortex ring was presumably formed out of the primary vortex ring induced vorticity at the annulus edge and the primary vortex ring was believed to break down upon impact. The experimental results reveal that the increase in the vortex ring circulation leads to

an increase in plate deflection. The electrical energy harvested by IPMC was estimated from the short-circuit current output. Approximately 0.0001-0.001% of the initial vortex ring energy, evaluated with vortex ring thin core assumption, was converted to electrical energy.

The experimental result was compared with an analytical model. The analytical framework neglected the small deflection of the annulus. It modeled the annulus' influence in the fluid domain as a rigid circular aperture in an infinite plane with an axisymmetric potential flow solution. The IPMC was represented with a linearized plate model. The inviscid flow solution neglects any viscous effects, thus it does not predict the secondary vortex ring generation and breakdown of the primary vortex ring. Overall, the analytical solution agrees well with the experimental results, and it provides a groundwork for the future energy harvesting capacity estimation.

Chapter 5

Recommendations

From the experiences gathered from the study, the author makes the following recommendations for future research regarding each energy harvesting configuration.

5.1 Vortex ring passing by a cantilevered deformable plate configuration recommendations

1. The current study focused on the scenario of a single vortex ring. Goushcha *et al.* [76] experimentally demonstrated that resonances can be achieved by matching the time interval between multiple vortices and the plate's natural frequency. The result of the present study established that the convective time scale plays a critical role in the interaction; thus, it would be of interest to examine the influence of the convective time scale on the resonances frequency for the multiple vortex ring scenario.

Additionally, the fluid-structure coupling behaviours should also be examined for the multiple vortex ring scenario.

2. In the scenario of multiple passing vortex rings, leapfrogging phenomena occurs if the interval between vortex rings is within certain ranges depending on the Reynolds number [55]. Examining the influence of the additional vortex-vortex interaction to vortex-deformable structure interaction can provide further insights into more complex interactions in turbulent driven harvesters.

3. The current study assumed an ideal fluid; consequently, the induced vorticity at the wall [70], vortex core distortion [118], vortex stretching [69], tip vortices [95] and the interaction between these phenomena were all neglected. Numerical and experimental investigation of the viscous effects will demonstrate the energy harvesting capability when the vortex ring is close to the plate.

4. The current study only examined the energy transfer of the vortex-deformable structure interaction, and Goushcha *et al.* [76] only used a strain gauge as a surrogate for piezoelectric materials, which seems to have impacted the beam dynamics. There is not any study of this particular energy harvesting configuration that examines the energy harvesting capabilities with actual smart materials. A study with piezoelectrics and IPMC should be performed to demonstrate the feasibility, as well as to examine how the electro-mechanical coupling alters the fluid-structure interaction.

5. A vortex ring passing by a cantilevered plate energy harvesting configuration was examined in the present study, while direct orthogonal impact on a cantilevered

plate was examined previously by Peterson and Porfiri [72]. By extension, the energy harvesting potential of a vortex ring impacting a cantilevered plate at an angle should also be studied. Additionally, Lim experimentally demonstrated very interesting vortex dynamics when a vortex ring impinges on an inclined wall [69]. He showed that bi-helical vortex lines formed due to variation in the rate of vortex stretching which then compressed to the region of the vortex ring that is furthest from the wall. Examining how a deformable wall influence this process will contribute to the fundamental understanding of vortex-deformable structure interaction.

5.2 Vortex ring impacting a deformable annulus configuration recommendations

1. Due to the IPMC fixture, the interaction between the vortex ring and the annulus was not captured. To advance the understanding of the vortex dynamics, an additional investigation should be performed. Since the annulus deflection is relatively small compared to its size, the annulus can be replaced with a rigid wall, thus eliminating the fixture. Consequently, flow visualization and PIV measurements can be implemented. Additionally, Miloh illustrated that a vortex ring traveling coaxially towards an annulus can either pass through or be blocked by it depending on the ring, core and annulus radius in an ideal fluid [104]. Investigating how the viscous effects change the limit between the passing and blocking cases is beneficial for further understanding the role of viscosity in fluid-structure interaction.

2. During the experiment, the author noticed that when the centers of the annulus and the vortex ring are not concentrically aligned, the secondary vortex ring convects out of the annulus at an angle. Furthermore, as mentioned in §5.1, bi-helical vortex lines are formed and compressed when the vortex ring is impacting a rigid wall at an angle. It is appealing to examine the influence of the cutout on the vortex dynamics, and the formation of the secondary vortex ring. It is important to explore the above scenarios in order to demonstrate the feasibility and potential of this energy harvesting configuration in real life conditions.

3. The formation of the secondary vortex ring hints at the possibility of secondary energy harvesting to increase the harvesting efficiency. With this intention, multiple annuli can be arranged in a cascade manner. This includes investigating the change in the secondary vortex ring properties with respect to the annulus and the primary vortex ring, as well as the influences of the secondary annulus on the formation of the secondary vortex ring.

4. The stretching of the annulus as it deflects adds extra rigidity to the structure. To achieve maximum deflection for optimal energy harvesting efficiency, the annulus can be cut into a circular array of smart material elements, see Figure 5.1. This allows the plate to vibrate similar to a cantilevered plate. It would be beneficial to study the vortex dynamics of this interaction, as well as the influence of geometry parameters (cutout radius R_i, fixture radius R_o, gap length L_g and number of element n) on the hydrodynamic loading and vortex-structure interaction for optimization.
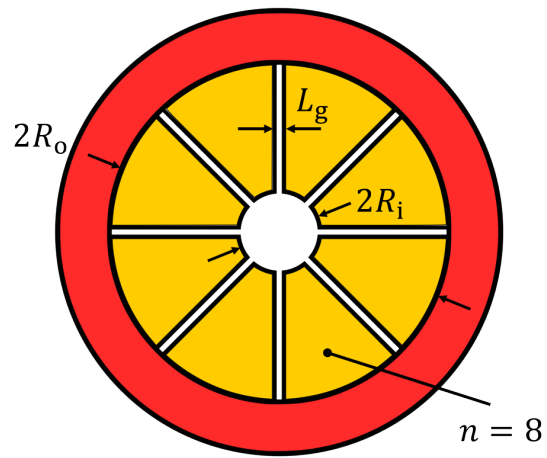
Figure 5.1: Circular array of smart materials as new annulus energy harvester design. Red color indicates the fixture and gold color indicates the smart material.

Bibliography

[1] J. Rabaey, J. Ammer, B. Otis, F. Burghardt, Y. H. Chee, N. Pletcher, M. Sheets, and H. Qin, "Ultra-low-power design," *IEEE Circuits and Devices Magazine*, vol. 22, no. 4, pp. 23–29, 2006.

[2] J. M. Rabaey, M. J. Ammer, J. L. J. Da Silva, D. Patel, and S. Roundy, "PicoRadio supports ad hoc ultra-low power wireless networking," *Computer*, vol. 33, no. 7, pp. 42–48, 2000.

[3] S. J. Roundy, *Energy Scavenging for Wireless Sensor Nodes with a Focus on Vibration to Electricity Conversion.* PhD thesis, University of California, Berkeley, 2003.

[4] Y. H. Chee, M. Koplow, M. Mark, N. Pletcher, M. Seeman, F. Burghardt, D. Steingart, J. Rabaey, P. Wright, and S. Sanders, "PicoCube: A 1 cm3 sensor node powered by harvested energy," in *Design Automation Conference*, (Anaheim, USA), pp. 114–119, IEEE, 2008.

[5] G. Chen, H. Ghaed, R. Haque, M. Wieckowski, Y. Kim, K. G., D. Fick, D. Kim, S. M., K. Wise, D. Blaauw, and D. Sylvester, "A cubic-millimeter energy-autonomous

wireless intraocular pressure monitor," in *IEEE International Solid-State Circuits Conference Digest of Technical Papers*, (San Francisco, CA), pp. 310–312, IEEE, 2011.

[6] S. Oshima, K. Matsunaga, T. Shimamura, H. Morimura, and M. Harada, "1-cm3 event-driven wireless sensor nodes," in *2012 IEEE International Conference on Communication Systems*, (Singapore), pp. 6–10, IEEE, 2012.

[7] M. Magno, D. Boyle, D. Brunelli, B. O'Flynn, E. Popovici, and L. Benini, "Extended Wireless Monitoring Through Intelligent Hybrid Energy Supply," *IEEE Transactions on Industrial Electronics*, vol. 61, no. 4, pp. 1871–1881, 2014.

[8] J. D. Hobeck, *Energy Harvesting with Piezoelectric Grass for Autonomous Self-Sustaining Sensor Networks*. PhD thesis, Unversity of Michigan, 2014.

[9] A. Erturk, *Electromechanical Modeling of Piezoelectric Energy Harvesters*. PhD thesis, 2009.

[10] A. Erturk and D. J. Inman, "An experimentally validated bimorph cantilever model for piezoelectric energy harvesting from base excitations," *Smart Materials and Structures*, vol. 18, no. 2, p. 025009, 2009.

[11] Y. Cha, H. Kim, and M. Porfiri, "Energy harvesting from underwater base excitation of a piezoelectric composite beam," *Smart Materials and Structures*, vol. 22, no. 11, p. 115026, 2013.

[12] K. A. Cook-Chennault, N. Thambi, and A. M. Sastry, "Powering MEMS portable devices - a review of non-regenerative and regenerative power supply systems with

special emphasis on piezoelectric energy harvesting systems," *Smart Materials and Structures*, vol. 17, no. 4, p. 043001, 2008.

[13] M. Shahinpoor and K. J. Kim, "Ionic polymer-metal composites: I. Fundemental," *Smart Materials and Structures*, vol. 10, no. 4, pp. 819–833, 2001.

[14] M. Aureli and M. Porfiri, "Low frequency and large amplitude oscillations of cantilevers in viscous fluids," *Applied Physics Letters*, vol. 96, no. 16, p. 164102, 2010.

[15] Y. Cha, M. Verotti, H. Walcott, S. D. Peterson, and M. Porfiri, "Energy harvesting from the tail beating of a carangiform swimmer using ionic polymer-metal composites," *Bioinspiration & biomimetics*, vol. 8, no. 3, p. 036003, 2013.

[16] Y. Cha, L. Shen, and M. Porfiri, "Energy harvesting from underwater torsional vibrations of a patterned ionic polymer metal composite," *Smart Materials and Structures*, vol. 22, no. 5, p. 055027, 2013.

[17] F. Cellini, Y. Cha, and M. Porfiri, "Energy harvesting from fluid-induced buckling of ionic polymer metal composites," *Journal of Intelligent Material Systems and Structures*, vol. 25, no. 12, pp. 1496–1510, 2014.

[18] Y. Cha, S. Abdolhamidi, and M. Porfiri, "Energy harvesting from underwater vibration of an annular ionic polymer metal composite," *Meccanica*, 2015.

[19] G. D. Bufalo, L. Placidi, and M. Porfiri, "A mixture theory framework for modeling the mechanical actuation of ionic polymer metal composites," *Smart Materials and Structures*, vol. 17, no. 4, p. 045010, 2008.

[20] Y. Cha, M. Aureli, and M. Porfiri, "A physics-based model of the electrical impedance of ionic polymer metal composites," *Journal of Applied Physics*, vol. 111, no. 12, p. 124901, 2012.

[21] The World Bank Group, "The world bank world development indicators," 2012.

[22] G. W. Taylor, J. R. Burns, S. M. Kammann, W. B. Powers, and T. R. Welsh, "The energy harvesting Eel: A small subsurface ocean/river power generator," *IEEE Journal of Oceanic Engineering*, vol. 26, no. 4, pp. 539–547, 2001.

[23] E. Bischur, S. Pobering, M. Menacher, and N. Schwesinger, "Flow driven vibration energy harvester," in *ASME 2010 Conference on Smart Materials, Adaptive Structures and Intelligent Systems*, (Pennsylvania, USA), p. 3736, 2010.

[24] X. Gao, W. H. Shih, and W. Y. Shih, "Flow Energy Harvesting Using Piezoelectric Cantilevers With Cylindrical Extension," *IEEE Transactions on Industrial Electronics*, vol. 60, no. 3, pp. 1116–1118, 2013.

[25] H. D. Akaydin, N. Elvin, and Y. Andreopoulos, "Energy Harvesting from Highly Unsteady Fluid Flows using Piezoelectric Materials," *Journal of Intelligent Material Systems and Structures*, vol. 21, no. 13, pp. 1263–1278, 2010.

[26] H. D. Akaydin, N. Elvin, and Y. Andreopoulos, "The performance of a self-excited fluidic energy harvester," *Smart Materials and Structures*, vol. 21, no. 2, p. 025007, 2012.

[27] J. Sirohi and R. Mahadik, "Harvesting Wind Energy Using a Galloping Piezoelectric Beam," *Journal of Vibration and Acoustics*, vol. 134, no. 1, p. 011009, 2012.

[28] J. Sirohi and R. Mahadik, "Piezoelectric wind energy harvester for low-power sensors," *Journal of Intelligent Material Systems and Structures*, vol. 22, no. 18, pp. 2215–2228, 2011.

[29] Y. Yang, L. Zhao, and L. Tang, "Comparative study of tip cross-sections for efficient galloping energy harvesting," *Applied Physics Letters*, vol. 102, no. 6, p. 064105, 2013.

[30] S. Li, J. Yuan, and H. Lipson, "Ambient wind energy harvesting using cross-flow fluttering," *Journal of Applied Physics*, vol. 109, no. 2, pp. 2013–2016, 2011.

[31] A. Giacomello and M. Porfiri, "Underwater energy harvesting from a heavy flag hosting ionic polymer metal composites," *Journal of Applied Physics*, vol. 109, no. 8, p. 084903, 2011.

[32] S. Michelin and O. Doaré, "Energy harvesting efficiency of piezoelectric flags in axial flows," *Journal of Fluid Mechanics*, vol. 714, pp. 489–504, 2013.

[33] J. D. Hobeck and D. J. Inman, "Artificial piezoelectric grass for energy harvesting from turbulence-induced vibration," *Smart Materials and Structures*, vol. 21, no. 10, p. 105024, 2012.

[34] J. Töger, M. Kanski, M. Carlsson, S. J. Kovács, G. Söderlind, H. Arheden, and E. Heiberg, "Vortex Ring Formation in the Left Ventricle of the Heart: Analysis by 4D Flow MRI and Lagrangian Coherent Structures," *Annals of Biomedical Engineering*, vol. 40, no. 12, pp. 2652–2662, 2012.

[35] G. V. Lauder, "Function of the Caudal Fin During Locomotion in Fishes: Kinematics, Flow Visualization, and Evolutionary Patterns," *American Zoologist*, vol. 40, no. 1, pp. 101–122, 2000.

[36] T. T. Lim, "On the breakdown of vortex rings from inclined nozzles," *Physics of Fluids*, vol. 10, no. 7, p. 1666, 1998.

[37] K. Mohseni, H. Ran, and T. Colonius, "Numerical experiments on vortex ring formation," *Journal of Fluid Mechanics*, vol. 430, pp. 267–282, 2001.

[38] M. Rosenfeld, E. Rambod, and M. Gharib, "Circulation and formation number of laminar vortex rings," *Journal of Fluid Mechanics*, vol. 376, pp. 297–318, 1998.

[39] C. Schram and M. L. Riethmuller, "Vortex ring evolution in an impulsively started jet using digital particle image velocimetry and continuous wavelet analysis," *Measurement Science and Technology*, vol. 12, no. 9, pp. 1413–1421, 2001.

[40] M. Gharib, E. Rambod, and K. Shariff, "A universal time scale for vortex ring formation," *Journal of Fluid Mechanics*, vol. 360, pp. 121–140, apr 1998.

[41] J. O. Dabiri and M. Gharib, "Fluid entrainment by isolated vortex rings," *Journal of Fluid Mechanics*, vol. 511, pp. 311–331, 2004.

[42] C. H. Liu, "Vortex simulation of unsteady shear flow induced by a vortex ring," *Computers & Fluids*, vol. 31, no. 2, pp. 183–207, 2002.

[43] I. S. Sullivan, J. J. Niemela, R. E. Hershberger, D. Bolster, and R. J. Donnelly, "Dynamics of thin vortex rings," *Journal of Fluid Mechanics*, vol. 609, pp. 319–347, jul 2008.

[44] T. Kambe and T. Takao, "Motion of distorted vortex rings," *Journal of the Physical Society of Japan*, vol. 31, no. 2, pp. 591–599, 1971.

[45] K. C. Stewart, C. L. Niebel, S. Jung, and P. P. Vlachos, "The decay of confined vortex rings," *Experiments in Fluids*, vol. 53, no. 1, pp. 163–171, 2012.

[46] M. E. Stern and L. J. Pratt, "Dynamics of vorticity," *Journal of Fluid Mechanics*, vol. 106, pp. 49–58, 1981.

[47] P. Chatelain, D. Kivotides, and A. Leonard, "Reconnection of colliding vortex rings," *Physical Review Letters*, vol. 90, no. 5, p. 054501, 2003.

[48] T. T. Lim and T. B. Nickels, "Instability and reconnection in the head-on collision of two vortex rings," *Nature*, vol. 357, no. 6375, pp. 225–227, 1992.

[49] T. T. Lim, B. K. Lua, and K. Thet, "Does Kutta lift exist on a vortex ring in a uniform cross flow?," *Physics of Fluids*, vol. 20, no. 5, pp. 19–23, 2008.

[50] M. Cheng, J. Lou, and T. T. Lim, "Vortex ring with swirl: A numerical study," *Physics of Fluids*, vol. 22, no. 9, p. 097101, 2010.

[51] M. Cheng, J. Lou, and T. T. Lim, "Motion of a vortex ring in a simple shear flow," *Physics of Fluids*, vol. 21, no. 8, p. 081701, 2009.

[52] N. Riley and D. P. Stevens, "A note on leapfrogging vortex rings," *Fluid Dynamics Research*, vol. 11, no. 5, pp. 235–244, 1993.

[53] A. V. Borisov, A. A. Kilin, I. S. Mamaev, and V. A. Tenenev, "The dynamics of vortex rings: leapfrogging in an ideal and viscous fluid," *Fluid Dynamics Research*, vol. 46, no. 3, p. 031415, 2014.

[54] J. Satti and J. Peng, "Leapfrogging of two thick-cored vortex rings," *Fluid Dynamics Research*, vol. 45, p. 035503, 2013.

[55] T. T. Lim, "A note on the leapfrogging between two coaxial vortex rings at low Reynolds numbers," *Physics of Fluids*, vol. 9, no. 1, pp. 239–241, 1997.

[56] S. E. Widnall, D. B. Bliss, and C. Y. Tsai, "The instability of short waves on a vortex ring," *Journal of Fluid Mechanics*, vol. 66, no. 1, pp. 35–47, 1974.

[57] V. F. Kop'ev, "Long-wave instability of a vortex ring," *Fluid Dynamics*, vol. 30, no. 6, pp. 864–869, 1995.

[58] Y. Fukumoto and Y. Hattori, "Curvature instability of a vortex ring," *Journal of Fluid Mechanics*, vol. 526, pp. 77–115, 2005.

[59] A. Weigand and M. Gharib, "On the decay of a turbulent vortex ring," *Physics of Fluids*, vol. 6, no. 12, p. 3806, 1994.

[60] A. Glezer and D. Coles, "An experimental study of a turbulent vortex ring," *Journal of Fluid Mechanics*, vol. 211, no. -1, p. 243, 2006.

[61] T. T. Lim, "On the role of Kelvin-Helmholtz-like instability in the formation of turbulent vortex rings," *Fluid Dynamics Research*, vol. 21, no. 1, pp. 47–56, 1997.

[62] H. Feng, L. Kaganovskiy, and R. Krasny, "Azimuthal instability of a vortex ring computed by a vortex sheet panel method," *Fluid Dynamics Research*, vol. 41, no. 5, p. 051405, 2009.

[63] T. Maxworthy, "Turbulent vortex rings," *Journal of Fluid Mechanics*, vol. 64, no. 2, pp. 227–239, 1974.

[64] T. T. Lim, T. B. Nickels, and M. S. Chong, "A note on the cause of rebound in the head-on collision of a vortex ring with a wall," *Experiments in Fluids*, vol. 12, no. 1-2, pp. 41–48, 1991.

[65] A. M. Naguib and M. M. Koochesfahani, "On wall-pressure sources associated with the unsteady separation in a vortex-ring/wall interaction," *Physics of Fluids*, vol. 16, no. 7, pp. 2613–2622, 2004.

[66] D. Adhikari and T. T. Lim, "The impact of a vortex ring on a porous screen," *Fluid Dynamics Research*, vol. 41, no. 5, p. 051404, 2009.

[67] Y. Jouanne and J. J. Allen, "Vortex interaction with a moving sphere," *Journal of Fluid Mechanics*, vol. 587, pp. 337– 346, 2007.

[68] M. Cheng, J. Lou, and T. T. Lim, "A numerical study of a vortex ring impacting a permeable wall," *Physics of Fluids*, vol. 26, no. 10, p. 103602, 2014.

[69] T. T. Lim, "An experimental study of a vortex ring interacting with an inclined wall," *Experiments in Fluids*, vol. 7, no. 7, pp. 453–463, 1989.

[70] J. D. A. Walker, C. R. Smith, A. W. Cerra, and T. L. Doligalski, "The impact of a vortex ring on a wall," *Journal of Fluid Mechanics*, vol. 181, pp. 99–140, 1987.

[71] D. G. Akhmetov, *Vortex rings.* Berlin; Heidelberg;: Springer-Verlag, 1 ed., 2009.

[72] S. D. Peterson and M. Porfiri, "Energy exchange between a vortex ring and an ionic polymer metal composite," *Applied Physics Letters*, vol. 100, no. 11, p. 114102, 2012.

[73] S. D. Peterson and M. Porfiri, "Interaction of a vortex pair with a flexible plate in an ideal quiescent fluid," *Journal of Intelligent Material Systems and Structures*, vol. 23, no. 13, pp. 1485–1504, 2012.

[74] S. D. Peterson and M. Porfiri, "Impact of a vortex dipole with a semi-infinite rigid plate," *Physics of Fluids*, vol. 25, no. 9, 2013.

[75] E. Zivkov, S. Yarusevych, M. Porfiri, and S. D. Peterson, "Numerical investigation of the interaction of a vortex dipole with a deformable plate," *Journal of Fluids and Structures*, vol. 58, pp. 203–215, 2015.

[76] O. Goushcha, N. Elvin, and Y. Andreopoulos, "Interactions of vortices with a flexible beam with applications in fluidic energy harvesting," *Applied Physics Letters*, vol. 104, 2014.

[77] S. Alben, "Interactions between vortices and flexible walls," *International Journal of Non-Linear Mechanics*, vol. 46, no. 4, pp. 586–591, 2011.

[78] S. Alben, "The attraction between a flexible filament and a point vortex," *Journal of Fluid Mechanics*, vol. 697, pp. 481–503, 2012.

[79] J. Hu, M. Porfiri, and S. D. Peterson, "Energy transfer between a passing vortex ring and a flexible plate in an ideal quiescent fluid," *Journal of Applied Physics*, vol. 118, no. 11, p. 114902, 2015.

[80] E. H. Mansfield, *The Bending and Stretching of Plates.* New York: Cambridge University Press, 2 ed., 1989.

[81] J. L. Humar, *Dynamics of Structures.* London, U.K.: Taylor & Francis Group, 2 ed., 2002.

[82] M. Aureli, C. Prince, M. Porfiri, and S. D. Peterson, "Energy harvesting from base excitation of ionic polymer metal composites in fluid environments," *Smart Materials and Structures*, vol. 19, no. 1, p. 015003, 2010.

[83] J. Hu, Y. Cha, M. Porfiri, and S. D. Peterson, "Energy harvesting from a vortex ring impinging on an annular ionic polymer metal composite," *Smart Materials and Structures*, vol. 23, no. 7, p. 074014, 2014.

[84] L. M. Milne-Thomson, *Theoretical Hydrodynamics.* New York: Dover Publications, 1996.

[85] G. K. Batchelor, *An Introduction to Fluid Dynamics.* Cambridge, U.K.: Cambridge University Press, 1967.

[86] S. Michelin and S. G. Llewellyn Smith, "Resonance and propulsion performance of a heaving flexible wing," *Physics of Fluids*, vol. 21, no. 7, p. 071902, 2009.

[87] S. S. Yoon and S. D. Heister, "Analytical formulas for the velocity field induced by an infinitely thin vortex ring," *International Journal for Numerical Methods in Fluids*, vol. 44, no. 6, pp. 665–672, 2004.

[88] Y. Andreopoulos, "Personal communication," 2014.

[89] Gilbert Curry Industrial Plastics Co Ltd, *Lexan 9030 Sheet*, 2015.

[90] Plastics International, *Makrolon GP (Ploycarbonate)*, 2015.

[91] SABIC Innovative Plastics, *Lexan SGC100 Sheet*, 2015.

[92] SABIC Innovative Plastics, *Lexan XL102UV Sheet*, 2015.

[93] General Electric Company, *Lexan 9034 Sheet*, 2015.

[94] H. D. Akaydin, N. Elvin, and Y. Andreopoulos, "Wake of a cylinder: A paradigm for energy harvesting with piezoelectric materials," *Experiments in Fluids*, vol. 49, no. 1, pp. 291–304, 2010.

[95] Y. H. Kim, S. T. Wereley, and C. H. Chun, "Phase-resolved flow field produced by a vibrating cantilever plate between two endplates," *Physics of Fluids*, vol. 16, no. 1, pp. 145–162, 2004.

[96] C. Prince, W. Lin, J. Lin, S. D. Peterson, and M. Porfiri, "Temporally-resolved hydrodynamics in the vicinity of a vibrating ionic polymer metal composite," *Journal of Applied Physics*, vol. 107, no. 9, p. 094908, 2010.

[97] C. A. Van Eysden and J. E. Sader, "Small amplitude oscillations of a flexible thin blade in a viscous fluid: Exact analytical solution," *Physics of Fluids*, vol. 18, no. 12, p. 123102, 2006.

[98] C. P. Green and J. E. Sader, "Torsional frequency response of cantilever beams immersed in viscous fluids with applications to the atomic force microscope," *Journal of Applied Physics*, vol. 84, no. 1, p. 64, 1998.

[99] A. L. Facci and M. Porfiri, "Analysis of three-dimensional effects in oscillating cantilevers immersed in viscous fluids," *Journal of Fluids and Structures*, vol. 38, pp. 205–222, 2013.

[100] M. Choi, C. Cierpka, and Y. H. Kim, "Vortex formation by a vibrating cantilever," *Journal of Fluids and Structures*, vol. 31, pp. 67–78, 2012.

[101] R. Shvydkoy, "On the energy of inviscid singular flows," *Journal of Mathematical Analysis and Applications*, vol. 349, no. 2, pp. 583–595, 2009.

[102] L. Meirovitch, *Fundamentals of Vibrations*. New York: McGraw-Hill Education, 1 ed., 2001.

[103] L. Fryba, *Vibration of solids and structures under moving loads*. London, U.K.: Thomas Telford, 3 ed., 1999.

[104] T. Miloh and D. J. Shlien, "Passage of a Vortex Ring through a Circular Aperture in an Infinite-Plane," *Physics of Fluids*, vol. 20, no. 1977, pp. 1219–1227, 1977.

[105] E. Elvin and A. Erturk, *Advances in Energy Harvesting Methods*. New York; Heidelberg; Dordrecht; London: Springer, 1 ed., 2013.

[106] R. Verzicco and P. Orlandi, "Wall/vortex-ring interactions," *Applied Mechanics Review*, vol. 49, no. 10, pp. 447–461, 1996.

[107] D. Ghosh and J. D. Baeder, "Numerical Simulation of Vortex Ring Interactions with Solid Wall," in *49th AIAA Aerospace Sciences Meeting including the New Horizons Forum and Aerospace Exposition*, (Orlando, USA), p. 675, 2011.

[108] A. W. Leissia, "Vibration of Plates," tech. rep., NASA, Washington, USA, 1969.

[109] M. Aureli, M. E. Basaran, and M. Porfiri, "Nonlinear finite amplitude vibrations of sharp-edged beams in viscous fluids," *Journal of Sound and Vibration*, vol. 331, no. 7, pp. 1624–1654, 2012.

[110] M. Amabili, G. Frosali, and M. Kwak, "Free Vibrations of Annular Plates Coupled with Fluids," *Journal of Sound and Vibration*, vol. 191, no. 5, pp. 825–846, 1996.

[111] C. Bonomo, L. Fortuna, P. Giannone, S. Graziani, and S. Strazzeri, "A nonlinear model for ionic polymer metal composites as actuators," *Smart Materials and Structures*, vol. 16, pp. 1–12, 2007.

[112] K. M. Newbury and D. J. Leo, "Linear Electromechanical Model of Ionic Polymer Transducers -Part I: Model Development," *Journal of Intelligent Materials Systems and Structures*, vol. 14, pp. 333–342, 2003.

[113] K. M. Newbury and D. J. Leo, "Journal of Intelligent Material Systems and Structures Linear Electromechanical Model of Ionic Polymer Transducers Part II : Experimental Validation," *Journal of Intelligent Material Systems and Structures*, vol. 14, pp. 343–357, 2003.

[114] M. Raffel, C. E. Willert, S. T. Wereley, and J. Kompenhans, *Particle Image Velocimetry: A Practical Guide.* Berlin; Heidelberg; New York: Springer, 2 ed., 2007.

[115] R. J. Adrian and J. Westerweel, *Particle Image Velocimetry.* New York, USA: Cambridge University Press, 2010.

[116] J. Y. Li and S. Nemat-nasser, "Micromechanical analysis of ionic clustering in Nafion perfluorinated membrane," *Mechanics of Materials*, vol. 32, no. 5, pp. 303–314, 2000.

[117] K. M. Farinholt, N. a. Pedrazas, D. M. Schluneker, D. W. Burt, and C. R. Farrar, "An Energy Harvesting Comparison of Piezoelectric and Ionically Conductive Polymers," *Journal of Intelligent Material Systems and Structures*, vol. 20, no. 5, pp. 633–642, 2008.

[118] E. R. Johnson and N. Robb McDonald, "Vortices near barriers with multiple gaps," vol. 531, pp. 335–358, 2005.